Atmospheric Research 292 (2023) 106857

Contents lists available at ScienceDirect

Atmospheric Research

journal homepage: www.elsevier.com/locate/atmosres

Dynamical analysis of multi-scale interaction during the “21·7” persistent rainstorm in Henan

Jiayi Liu [a], Li Tao [a,b,*], Yang Yang [c]

[a] School of Atmospheric Sciences/Collaborative Innovation Center on Forecast and Evaluation of Meteorological Disasters (CIC-FEMD), Nanjing University of Information Science & Technology, Nanjing, Jiangsu 210044, China
[b] State Key Laboratory of Severe Weather, Chinese Academy of Meteorological Sciences, Beijing 100081, China
[c] State Key Laboratory of Marine Environmental Science, College of Ocean and Earth Sciences, Xiamen University, Xiamen, China

ARTICLE INFO

Keywords:
“21•7” torrential rainfall event
Localized multiscale energetics
Barotropic instability
Baroclinic instability

ABSTRACT

This study explored the multiscale dynamical processes and energy contributions to the “21•7” torrential rainfall event (TRE), which hit Zhengzhou on July 20, 2021. Using a localized, instantaneous energetics diagnostic tool: the multiscale window transform (MWT) and MWT-based energy and vorticity analysis (MS-EVA), three scales fields: basic-flow fields (>64 days), intraseasonal oscillation fields (8–64 days) and synoptic-scale-eddy fields (<8 days) were obtained. An inverted trough over “21•7” TRE area on the scale of 8–64 days and a mesoscale high in front of Typhoon In-Fa (2021) on the scale of <8 days were identified by the MWT. There was persistent energy conversion from available potential energy (APE) to kinetic energy (KE) represented by the buoyancy term in the last 12 h and throughout the occurrence of the exceptional rainstorm. Latent heating was an important source of APE 12 h prior to the rainstorm. In addition to buoyancy conversion, a downscale energy cascade process of KE (barotropic instability) above 500 hPa was another source of KE prior to the rainstorm. During the rainstorm’s occurrence, the downscale energy cascade process of APE (baroclinic instability) at middle levels was the major source of APE. KE decreased significantly owing to eddy dissipation and diffusion at middle levels and the divergence of KE fluxes at low levels. The work done by the pressure gradient force was negligible for KE.

1. Introduction

An exceptionally heavy rainstorm during July 17–22, 2021, flooded cities including Zhengzhou, Weihui, Xinxiang, and Hebi, in Henan Province, China, with a maximum 6-day accumulated rainfall of 1122.6 mm in Hebi and maximum hourly rainfall of 201.9 mm in Zhengzhou from 08:00 to 09:00 UTC on July 20, which was the largest hourly rainfall observed in mainland of China. The torrential rain caused 14 deaths on Zhengzhou’s Metro Line 5 and breached the Communist Canal in its Xinxiang and Hebi sections. The urban areas of Weihui and Xinxiang were flooded for 7 days; 398 people were recorded as dead or missing because of the various disasters linked to the rainstorm; and, according to the *“July 20” Torrential Rain Disaster Investigation Report in Zhengzhou, Henan Province* by the Disaster Investigation Team of the State Council of China, January 2022, there were direct economic losses of up to 120.6 billion Yuan. The persistent rainstorm was named the “21•7” torrential rainfall event (TRE) in China.

Some studies suggested that the 21•7 TRE was caused by the joint effects of multi-scale atmospheric systems in the middle and low latitudes, including an abnormal northward shift of the western Pacific subtropical high, the westward-moving typhoon In-Fa, the northward-moving typhoon Cempaka, an upper-tropospheric trough and a quasi-stationary mesoscale vortex at low level (Ran et al., 2021; Liang et al., 2022; Zhang et al., 2021; Yu et al., 2022; Xu et al., 2022; Deng et al., 2022; Wei et al., 2023; Luo and Du, 2023; Zhang et al., 2023; Hu et al., 2023). Deng et al. (2022) addressed that the easterly flow, which prevailed between Typhoon In-Fa and the subtropical high, transported water vapor to the target area at 850 hPa, while the southwesterly flow was nonnegligible. Xu et al. (2022) emphasized the southerly flow, which prevailed between typhoon Cempaka and Henan, determined the structure and distribution of the 21•7 TRE. Zhang et al. (2023) identified two water vapor supply channels with backward trajectory tracking analysis. Based on radar observations and a convection-permitting simulation, Wei et al. (2023) suggested that Zhengzhou record-

---

* Corresponding author at: School of Atmospheric Sciences, Nanjing University of Information Science & Technology, Nanjing, Jiangsu Province 210044, China.
E-mail address: taoli@nuist.edu.cn (L. Tao).

https://doi.org/10.1016/j.atmosres.2023.106857
Received 17 February 2023; Received in revised form 5 June 2023; Accepted 6 June 2023

breaking hourly rainfall was caused by a single quasi-stationary storm associated with a low-level mesoscale vortex. Fu et al. (2022) also proposed that a long-lasting (21h) northwestward-moving mesoscale convective vortex and its interaction with its parent mesoscale convective system was crucial to producing the 21•7 TRE. Zhang et al. (2023) suggested the upper-tropospheric divergent flow between two potential vorticity streamers over Henan Province facilitated development of the deep mesoscale convective vortex. Hu et al. (2023) pointed out that northward shift of low-level component of the western Pacific subtropical high in July 2021 broke the record held since 1979.

Generally, TREs are difficult to forecast owing to their suddenness. Usually, they are a product of the interaction of multi-scale systems, especially super-heavy rain or persistent heavy rain. Not only can a convective-scale system occur and grow within a synoptic-scale system, but it can also feed back to that synoptic-scale system after the convection has developed (Ding, 2014). The interactions between different scale systems involve nonlinear processes, so they are highly complex and involve sudden changes (Tao, 1980; Ding, 2014). Therefore, how to quantitatively analyze the interaction between different scale systems remains a challenging issue.

Previous studies have examined the multi-scale interactions of heavy rainfall. For instance, Tao (1980) outlined a total of 11 large-scale circulations favorable for heavy rainfall. Based on scale analysis and energy budget calculations, Zhao et al. (2003) analyzed the effect of large-scale, low-level winds on the formation and development of the mesoscale low-level jet in a heavy rainfall event. Results showed that the kinetic energy (KE) associated with the low-level jet came from the work done by the reinforced synoptic-scale pressure gradient force. The KE then transferred upwards when the low-level jet formed. Zhang et al. (2008) identified meso-scale systems based on the Barnes filter (Barnes, 1964) and discussed the interaction between typhoon Haitang (2005) and the simultaneous large-scale mid-latitude system that was responsible for a rainstorm in Henan. Fu et al. (2016) simulated a persistent heavy rainfall event and analyzed the interaction between the mean flow and eddy based on the KE budget, revealing that the energy cascade processes of the KE were different in different layers. Majda and Stechmann (2009) developed a simple dynamic model to demonstrate the nonlinear interactions between the large-scale zonal mean flow and convectively coupled gravity waves, which cause the mean flow to oscillate on the intraseasonal scale. Note, however, that the eddy KE budget equation used in Zhao et al. (2003) and Fu et al. (2016) consisted only of the interaction between the eddy and the mean flow.

Hsu and Li (2011) decomposed fields into three scales by using the Butterworth filter and conducted a quantitative analysis of multi-scale energy exchange. However, they took the intraseasonal variation of the energy disturbed by the synoptic scale as the energy of intraseasonal oscillation (the Madden–Julian Oscillation), which not only incorrectly defined the multi-scale energy but also failed to guarantee the conservation of energy. Shen et al. (2018a) reviewed the literature on multiscale interactions, including Eliassen–Palm flux, wave packet theory, and atmospheric energetics. Shen et al. (2018b) derived a three-scale KE equation and potential energy equation. Sha et al. (2018) followed up that work by simulating a typical Meiyu front rainstorm and divided the fields into three scales by using the Barnes filter and quantitatively analyzed the transport and transfer energies between the three scales. However, the results were not only extremely complex but also failed to guarantee the conservation of energy.

The traditional temporally or spatially averaged energy diagnostic approach is not suitable for rainstorm events, as they are highly localized and rapidly developing weather systems. Liang and Anderson (2007) and Liang (2016) overcame this difficulty by introducing the multiscale window transform (MWT) and MWT-based multiscale energy and vorticity analysis (MS-EVA; Liang and Robinson, 2005; Liang and Anderson, 2007), which are scale-window based and localized in both space and time. One advantage of the MS-EVA approach over existing energetics formalisms is that it takes into account the issue of energy conservation among scales. The scale interaction term in the MS-EVA equations is simply a redistribution of energy among scale windows, referred to as "canonical transfer" by Liang and Anderson (2007), and therefore is a faithful representation of the real multiscale interaction processes. In this study, we applied this method to investigate the mechanisms of the rapid development of the 21•7 TRE and the interactions between the three scales.

The rest of the paper is organized as follows. Section 2 describes the data and methods used. Section 3 describes the prevailing weather system during the 21•7 TRE. Section 4.1 reconstructs the basic-flow fields (>64 days), intraseasonal oscillation fields (8–64 days), and synoptic-scale-eddy fields (<8 days). The results of the multiscale energetics analysis are discussed in Section 4.2, and conclusions are given in Section 5.

2. Data and methods

2.1. Data

The hourly precipitation data were obtained from 1893 observation stations across China, supplied by the National Meteorological Information Center, China Meteorological Administration (CMA, https://data.cma.cn/;Fig. 1).

The 6-hourly reanalysis data from the fifth major global reanalysis produced by the European Centre for Medium-Range Weather Forecasts (ERA5; Hersbach et al., 2020), with a horizontal resolution of 0.25° × 0.25° and 37 pressure levels, were used to produce the anomaly maps in Figs. 2 and 3. Meanwhile, the 6-hourly FNL (Final) Operational Model Global Tropospheric Analyses of the National Centers for Environmental Prediction (NCEP), with a horizontal resolution of 1.0° × 1.0° and 21 pressure levels (https://rda.ucar.edu/datasets/ds083.2/), were used for the MWT and energy analysis. We use FNL rather than ERA5 for this purpose because the rainfall intensity over TRE center in FNL was closer to the observation, even though the resolution of FNL is coarser than that of ERA5.

We chose the time span from 00:00 UTC March 23 to 18:00 UTC December 3, 2021, for conducting the MWT analysis. This gave a total of 1024 (2^{10}) time steps and was a power of 2, as required by MWT analysis, and was long enough to avoid possible boundary effects. The MWT were applied to each grid in the domain (−5.0°–80.0°N, 50.0°–160.0°E). There were several rainstorm processes during July 17–23, 2021. The centers of each process were located in different area. The domain (34.0°–36.5°N, 112.0°–114.5°E) covered these centers, and earmarked by rectangles as rainstorm area in Fig. 1-10, in order to facilitate analysis of the relative position of each weather system to the precipitation area. The small domain (34.0°–35.0°N, 113.0°–114.0°E) was selected to analyze the exceptional rainstorm that occurred in Zhengzhou from 00:00 UTC 20 to 00:00 UTC 21 July.

2.2. Methods

Unlike traditional filters, MWT yields not only reconstructions (i.e., filtered fields) but also transform coefficients, which are essential to define the energy associated with a filtered field. Liang and Anderson (2007) developed MWT for this purpose. MWT orthogonally decomposes a function space into several scale windows based on some orthonormal wavelet function, retaining the temporal locality of the multiscale energies. Given a time series $T(t)$ and scale window ϖ, $T(t)$ can be reconstructed onto the window, denoted as $T^{\sim\varpi}(t)$ (similar to a general filter). For each $T^{\sim\varpi}(t)$, there is a corresponding time-dependent transform coefficient, denoted as $\widehat{T}_n^{\sim\varpi}$. The multiscale energy on window ϖ is proportionate to $\left(\widehat{T}_n^{\sim\varpi}\right)^2$. Note that it is not simply the square of the filtered field (i.e., $\left[T^{\sim\varpi}\right]^2$), as commonly used in the literature. The subscript n denotes the discrete time step in the sampling space, which is omitted hereafter for brevity.

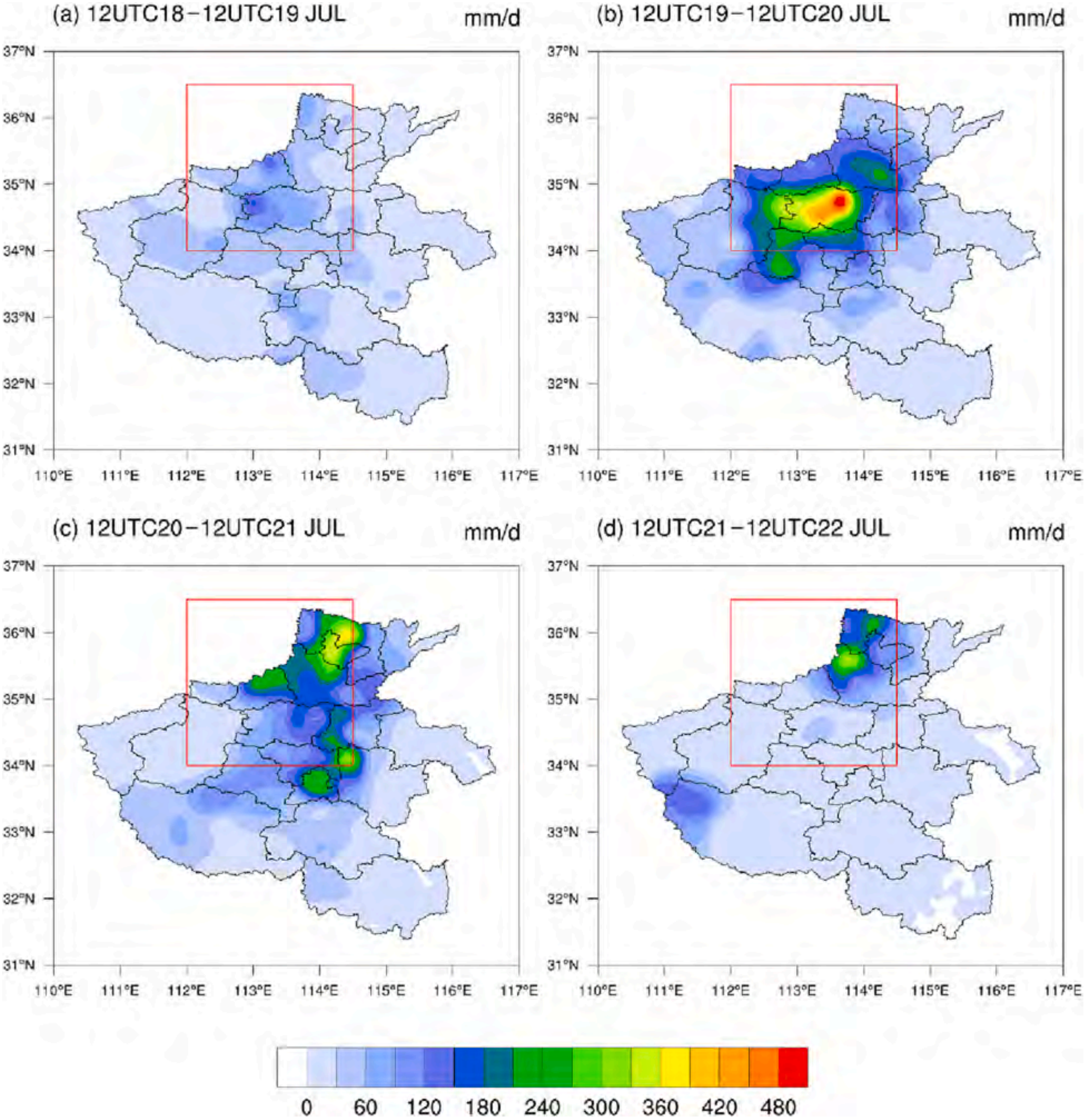

Fig. 1. Observed accumulative daily precipitation (mm/d) during (a) 12:00 UTC 18 to 12:00 UTC 19, (b) 12:00 UTC 19 to 12:00 UTC 20, (c) 12:00 UTC 20 to 12:00 UTC 21, and (d) 12:00 UTC 21 to 12:00 UTC 22, during the 7•21 TRE, obtained from the CMA. The red frames represent the domain (34.0°–36.5°N, 112.0°–114.5°E), which covers the rainfall centers. (For interpretation of the references to colour in this figure legend, the reader is referred to the web version of this article.)

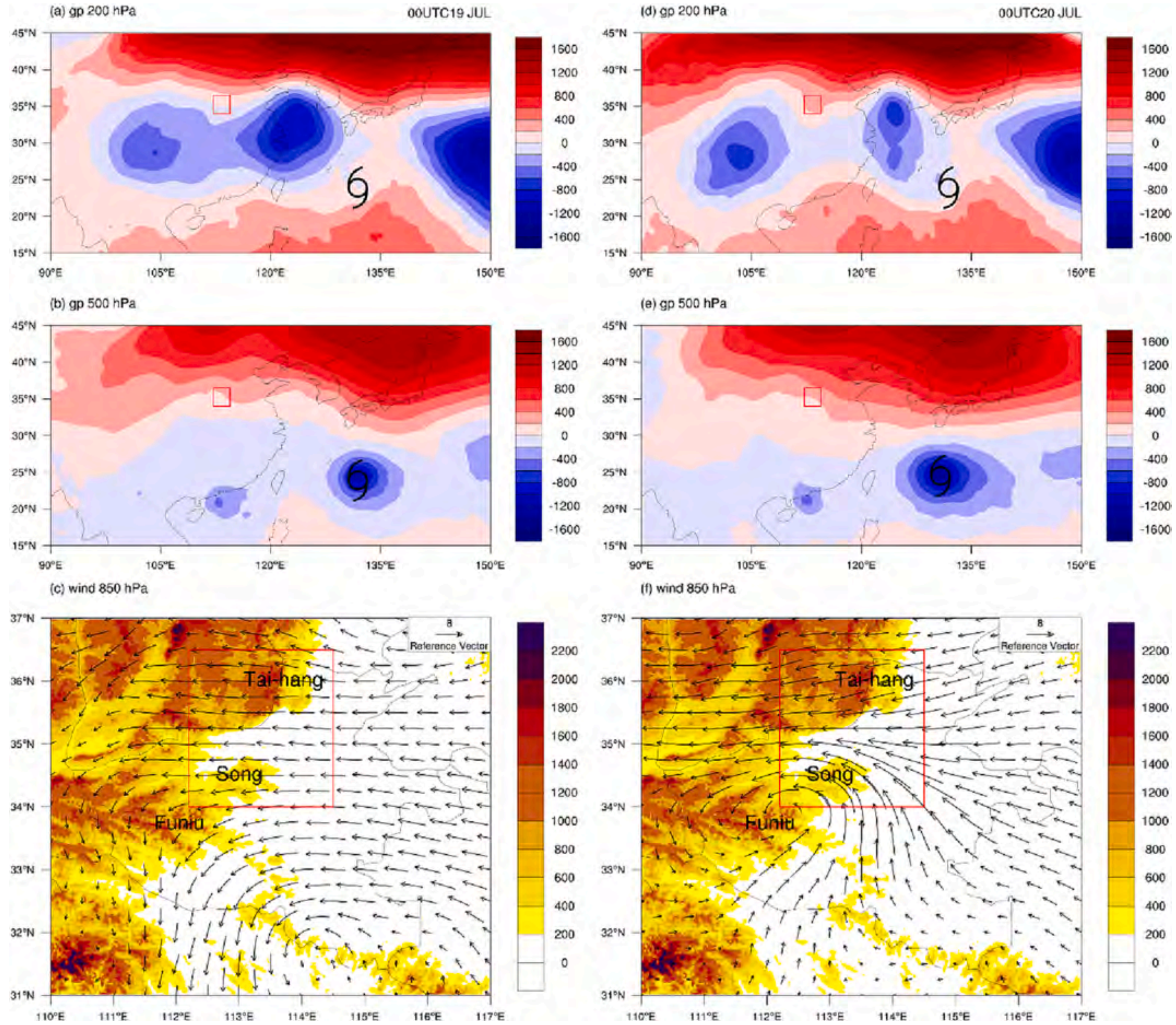

Fig. 2. The geopotential height anomalies relative to the monthly climatology averaged from 1979 to 2021 at (a, d) 200 hPa, (b, e) 500 hPa, and (c, f) the wind anomalies at 850 hPa superimposed with terrain height (shaded; m), on July 19 (left column) and July 20 (right column) obtained from ERA5. The red frames represent the domain (34.0°–36.5°N, 112.0°–114.5°E), which covers the rainfall centers. (For interpretation of the references to colour in this figure legend, the reader is referred to the web version of this article.)

The KE and available potential energy (APE) on the scale window ϖ are as following (Liang and Robinson, 2005; Liang, 2016):

$$K^{\varpi} = \frac{1}{2}\widehat{\boldsymbol{V}}_h^{\sim\varpi} \bullet \widehat{\boldsymbol{V}}_h^{\sim\varpi} \tag{1}$$

and

$$A^{\varpi} = \frac{1}{2}c\left(\widehat{\boldsymbol{T}}_h^{\sim\varpi}\right)^2, \tag{2}$$

where $c = \frac{g}{\overline{T}\left(\frac{g}{cp}-\gamma\right)}$, γ is the lapse rate, $\frac{g}{c_p}$ is lapse rate for dry air, $\overline{T}$ is the temperature averaged over the p plane. The evolution equations for K^{ϖ} and A^{ϖ} are as following:

$$\frac{\partial K^{\varpi}}{\partial t} + \underbrace{\nabla \bullet \left[\frac{1}{2}\widehat{(vv_h)}^{\sim\varpi} \bullet \widehat{v}_h^{\sim\varpi}\right]}_{\nabla \bullet Q_K^{\varpi}} = \underbrace{\frac{1}{2}\left\{\widehat{(vv_h)}^{\sim\varpi} : \nabla \widehat{v}_h^{\sim\varpi} - \left[\nabla \bullet \widehat{(vv_h)}^{\sim\varpi}\right] \bullet \widehat{v}_h^{\sim\varpi}\right\}}_{\Gamma_K^{\varpi}} - \underbrace{\nabla \bullet \left(\widehat{v}^{\sim\varpi}\widehat{\Phi}^{\sim\varpi}\right)}_{\nabla \bullet Q_P^{\varpi}} - \underbrace{\widehat{\omega}^{\sim\varpi}\widehat{\alpha}^{\sim\varpi}}_{b^{\varpi}} + F_K^{\varpi} \tag{3}$$

and

$$\frac{\partial A^{\varpi}}{\partial t} + \underbrace{\nabla \bullet \left[\frac{1}{2}c\widehat{(v\mathrm{T})}^{\sim\varpi}\widehat{T}^{\sim\varpi}\right]}_{\nabla \bullet Q_A^{\varpi}} = \underbrace{\frac{c}{2}\left[\widehat{(vT)}^{\sim\varpi} \bullet \nabla \widehat{T}^{\sim\varpi} - \widehat{T}^{\sim\varpi}\nabla \bullet \widehat{(vT)}^{\sim\varpi}\right]}_{\Gamma_A^{\varpi}} + \underbrace{\widehat{\omega}^{\sim\varpi}\widehat{\alpha}^{\sim\varpi}}_{b^{\varpi}} + F_A^{\varpi} \tag{4}$$

where $\nabla \bullet Q_K^{\varpi}$ and $\nabla \bullet Q_A^{\varpi}$ are the divergence of the KE and APE fluxes

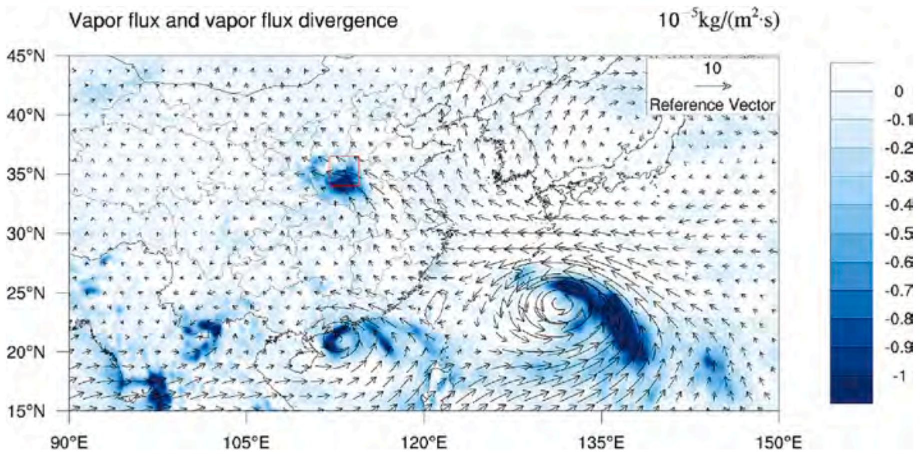

Fig. 3. Vertically integrated water vapor flux (vectors; 100 kg/(m·s)) from 1000 hPa to 300 hPa and water vapor flux divergence (shaded; 10^{-5} kg/(m^2·s)) averaged from July 19 to July 20. The red frame represents the domain (34.0°–36.5°N, 112.0°–114.5°E), which covers the rainfall centers. (For interpretation of the references to colour in this figure legend, the reader is referred to the web version of this article.)

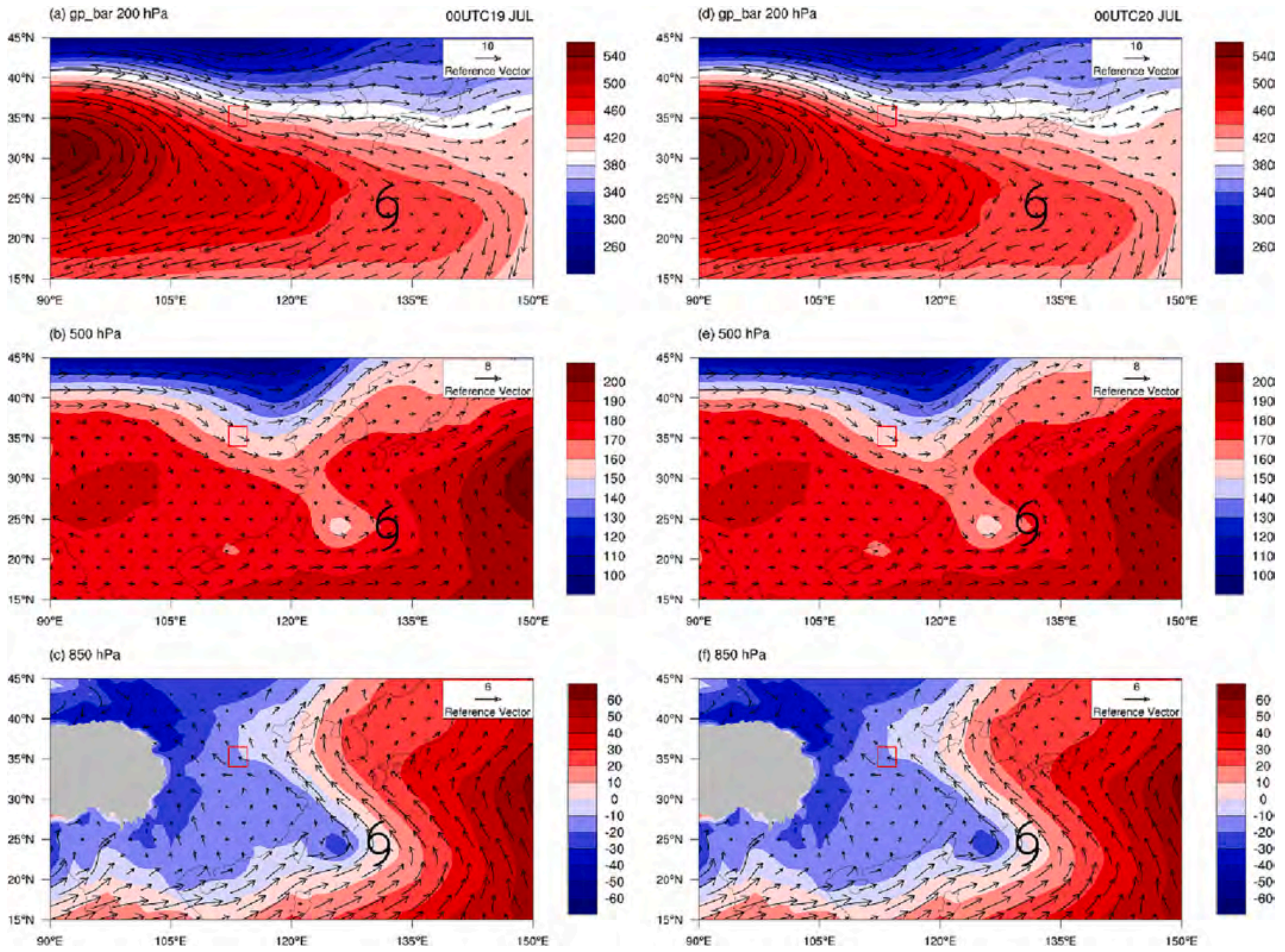

Fig. 4. The reconstructed geopotential height (shaded; gpm) and horizontal wind (vectors; m/s) at (a, d) 200 hPa, (b, e) 500 hPa and (c, f) 850 hPa on July 19 (left column) and July 20 (right column) on the basic-flow scale (>64 days) obtained by using MWT.

on the ϖ scale window, respectively; Γ_K^ϖ and Γ_A^ϖ are the canonical barotropic and baroclinic energy transfer to window ϖ, respectively; $\nabla \bullet Q_P^\varpi$ is the work done by the pressure gradient force; b^ϖ is the buoyancy conversion between the KE and the APE on window ϖ; F_K^ϖ is the residual term that represents the work done by eddy dissipation and diffusion; F_A^ϖ is the residual term that includes latent heating, sensible heating, and diffusion; and $\widehat{(\ )}^{\sim\varpi}$ is the MWT transform coefficient on scale window ϖ at time step n (the subscript n is omitted for brevity). The colon operator

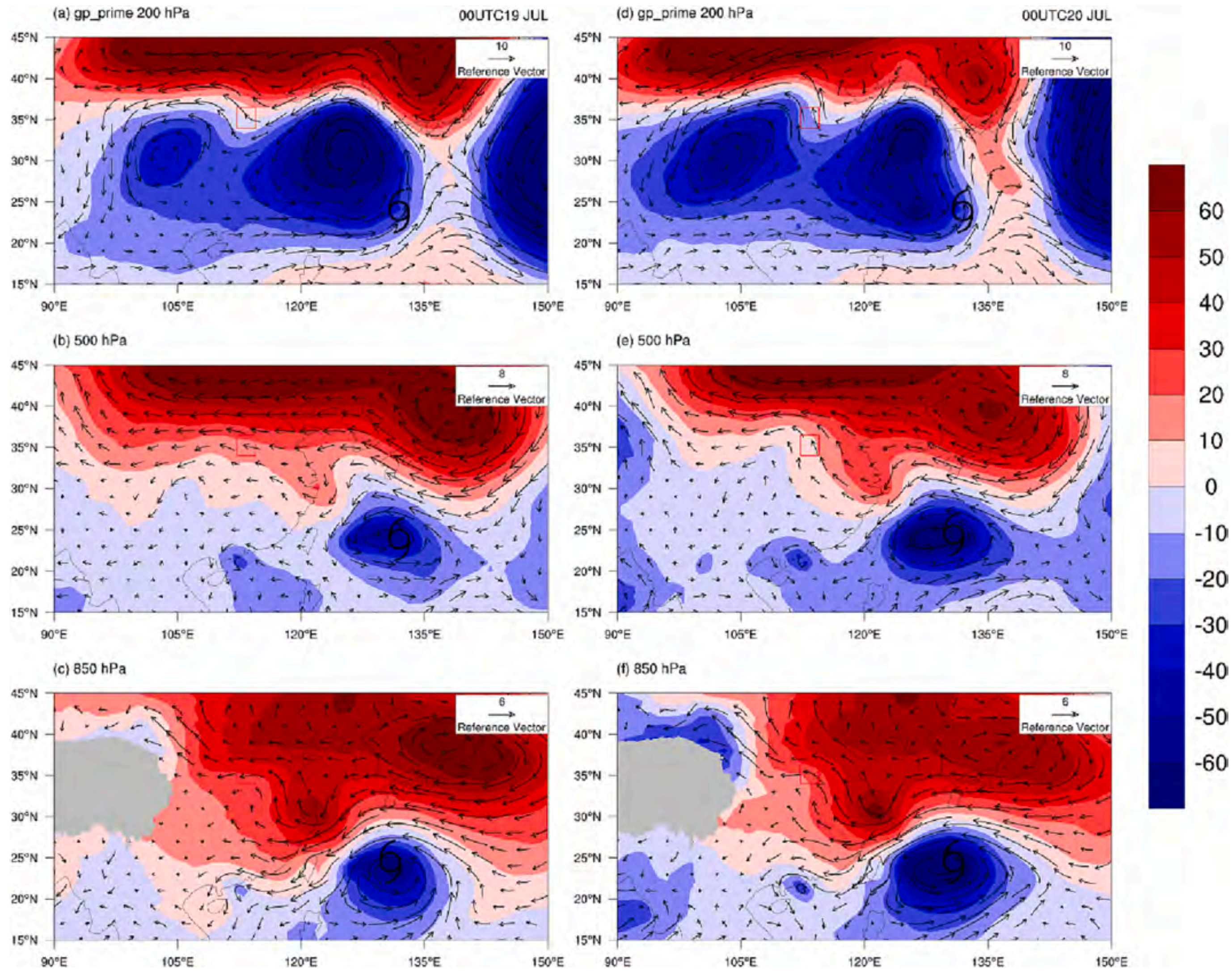

Fig. 5. The reconstructed geopotential height (shaded; gpm) and horizontal wind (vectors; m/s) at (a, d) 200 hPa, (b, e) 500 hPa and (c, f) 850 hPa on July 19 (left column) and July 20 (right column) on the intraseasonal scale (8–64 days) obtained by using MWT.

is defined such that for two dyadic products ***AB*** and ***CD***,

$$(\boldsymbol{AB}):(\boldsymbol{CD}) = (\boldsymbol{A}\bullet\boldsymbol{C})(\boldsymbol{B}\bullet\boldsymbol{D}) \tag{5}$$

Γ_K^{ϖ} on scale window ϖ at step n is generally understood as

$$\begin{aligned}\Gamma_K^{\varpi} =& \frac{1}{2}\left\{\left(\widehat{uu}^{\sim\varpi}\frac{\partial\widehat{u}^{\sim\varpi}}{\partial x}+\widehat{vu}^{\sim\varpi}\frac{\partial\widehat{u}^{\sim\varpi}}{\partial y}+\widehat{\omega u}^{\sim\varpi}\frac{\partial\widehat{u}^{\sim\varpi}}{\partial p}\right)\right.\\ &\left.-\left[\widehat{u}^{\sim\varpi}\left(\frac{\partial\widehat{uu}^{\sim\varpi}}{\partial x}+\frac{\partial\widehat{vu}^{\sim\varpi}}{\partial y}+\frac{\partial\widehat{\omega u}^{\sim\varpi}}{\partial p}\right)\right]\right\}\\ &+\frac{1}{2}\left\{\left(\widehat{uv}^{\sim\varpi}\frac{\partial\widehat{v}^{\sim\varpi}}{\partial x}+\widehat{vv}^{\sim\varpi}\frac{\partial\widehat{v}^{\sim\varpi}}{\partial y}+\widehat{\omega v}^{\sim\varpi}\frac{\partial\widehat{v}^{\sim\varpi}}{\partial p}\right)\right.\\ &\left.-\left[\widehat{v}^{\sim\varpi}\left(\frac{\partial\widehat{uv}^{\sim\varpi}}{\partial x}+\frac{\partial\widehat{vv}^{\sim\varpi}}{\partial y}+\frac{\partial\widehat{\omega v}^{\sim\varpi}}{\partial p}\right)\right]\right\}.\end{aligned} \tag{6}$$

All the terms on the right-hand side of Eq. (6) can be written as a linear combination of terms in the following triple product form:

$$\Gamma_K^{\varpi} = \widehat{R}^{\sim\varpi}\widehat{pq}^{\sim\varpi}. \tag{7}$$

For a three-window decomposition $\varpi = 0, 1, 2$, taking $\varpi = 2$, for example, Γ_n^{ϖ} can be decomposed as

$$\begin{aligned}\Gamma_K^{\varpi} = \Gamma_K^{2} = \widehat{R}^{\sim2}\widehat{pq}^{\sim2} &= \widehat{R}^{\sim2}\widehat{\left(\sum_{\varpi_1=0}^{2}p^{\sim\varpi_1}\sum_{\varpi_2=0}^{2}q^{\sim\varpi_2}\right)}^{\sim2}\\ &= \widehat{R}^{\sim2}\left[\left(\widehat{p^{\sim0}q^{\sim0}}\right)^{\sim2}+\left(\widehat{p^{\sim0}q^{\sim2}}\right)^{\sim2}+\left(\widehat{p^{\sim2}q^{\sim0}}\right)^{\sim2}\right]\\ &\quad+\widehat{R}^{\sim2}\left[\left(\widehat{p^{\sim1}q^{\sim1}}\right)^{\sim2}+\left(\widehat{p^{\sim1}q^{\sim2}}\right)^{\sim2}+\left(\widehat{p^{\sim2}q^{\sim1}}\right)^{\sim2}\right]\\ &\quad+\widehat{R}^{\sim2}\left[\left(\widehat{p^{\sim0}q^{\sim1}}\right)^{\sim2}+\left(\widehat{p^{\sim1}q^{\sim0}}\right)^{\sim2}\right]+\widehat{R}^{\sim2}\left[\left(\widehat{p^{\sim2}q^{\sim2}}\right)^{\sim2}\right].\end{aligned} \tag{8}$$

The first term, $\widehat{R}^{\sim2}\left[\left(\widehat{p^{\sim0}q^{\sim0}}\right)^{\sim2}+\left(\widehat{p^{\sim0}q^{\sim2}}\right)^{\sim2}+\left(\widehat{p^{\sim2}q^{\sim0}}\right)^{\sim2}\right] = \Gamma_K^{0\to2}$, is the energy transfer from scale window 0 to scale window 2. The second term, $\widehat{R}^{\sim2}\left[\left(\widehat{p^{\sim1}q^{\sim1}}\right)^{\sim2}+\left(\widehat{p^{\sim1}q^{\sim2}}\right)^{\sim2}+\left(\widehat{p^{\sim2}q^{\sim1}}\right)^{\sim2}\right] = \Gamma_K^{1\to2}$, is the energy transfer from window 1 to window 2. The third term, $\widehat{R}^{\sim2}\left[\left(\widehat{p^{\sim0}q^{\sim1}}\right)^{\sim2}+\left(\widehat{p^{\sim1}q^{\sim0}}\right)^{\sim2}\right] = \Gamma_K^{0\oplus1\to2}$, is the combined contribution to Γ_K^2 from the two-scale window 0 and window 1, which is generally negligible. The last term, $\widehat{R}^{\sim2}\left[\left(\widehat{p^{\sim2}q^{\sim2}}\right)^{\sim2}\right] = \Gamma_K^{2\to2}$, is the canonical energy transfer from window 2 itself. In particular, Γ_K^{ϖ} has a very important property, which has been rigorously proved by Liang (2016):

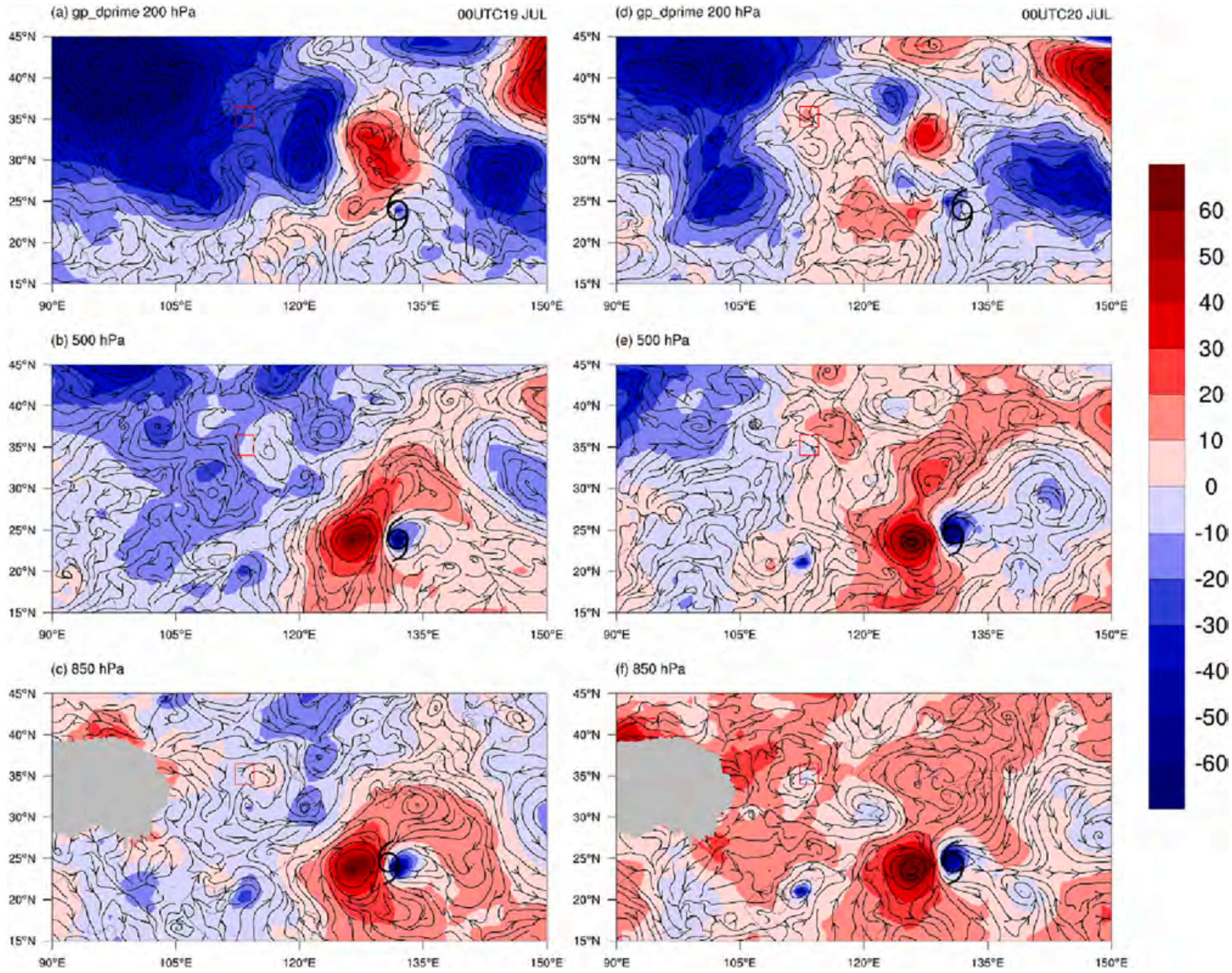

Fig. 6. The reconstructed geopotential height (shaded; gpm) and horizontal wind (stream lines) at (a, d) 200 hPa, (b, e) 500 hPa and (c, f) 850 hPa on July 19 (left column) and July 20 (right column) on the synoptic scale (<8 days) obtained by using MWT.

$$\sum_{\varpi}\left(\sum_{n}\Gamma_K^{\varpi}\right)=0. \tag{9}$$

This means that $\Gamma_K^{\varpi}$is simply a redistribution of KE among the scale windows without creating or consuming any energy. To distinguish it from the term of barotropic energy transfer, Γ_K^{ϖ} is referred to as “canonical barotropic energy transfer”. Likewise, Γ_A^{ϖ} is referred to as “canonical baroclinic energy transfer”. More details are available in Liang (2016). The software for MWT and MS-EVA and related references can be downloaded from http://www.ncoads.org/.

Based on the wavelet spectral analysis (Fig. S1) on the vertical velocity at 700 hPa averaged over the domain (34.0°-36.5°N, 112.0°-114.5°E), where the 21•7 TRE occurred, we decomposed and reconstructed the total field into three temporal scales by applying MWT: a window on the scale of basic flow (>64 days); a window on the scale of intraseasonal systems (8–64 days); and a window on the scale of synoptic scale eddies (<8 days), which are denoted as $\varpi = 0,1,2$, respectively. Moreover, for the energy transfer between the basic flow and rainstorm:

(1) If $\Gamma_K^{0\longrightarrow 2}+\Gamma_A^{0\longrightarrow 2}>0$, the basic flow is locally unstable;
(2) For an unstable system, if $\Gamma_K^{0\longrightarrow 2}>0$ and $\Gamma_A^{0\longrightarrow 2}\leq 0$, then the instability the basic flow undergoes is barotropic;
(3) For an unstable system, if $\Gamma_A^{0\longrightarrow 2}>0$ and $\Gamma_K^{0\longrightarrow 2}\leq 0$, then the instability of the basic flow is baroclinic; and
(4) If $\Gamma_K^{0\longrightarrow 2}>0$ and $\Gamma_A^{0\longrightarrow 2}>0$, mixing instability occurs.

These criteria are also held for the energy transfer between the intraseasonal flow and synoptic-scale eddy.

3. Weather system

3.1. *The rainstorm*

An exceptionally heavy rainstorm hit cities including Zhengzhou, Weihui, Xinxiang, and Hebi, in Henan Province, China, during 17–22 July 2021. The observed accumulated daily rainfall is shown in Fig. 1. In the period 12:00 UTC 18 through 12:00 UTC 19, the rainfall center was in the east of Zhengzhou. It intensified in the next 24 h, with the maximum rainfall in Zhengzhou exceeding 480 mm/day and the maximum hourly rainfall reaching 201.9 mm from 08:00 to 09:00 UTC on July 20. The rainfall center then moved northwards to Anyang and Hebi, with the maximum rainfall reaching 390 mm/day on July 21.

The domain (34.0°–36.5°N, 112.0°–114.5°E) covering the rainfall centers was chosen, and the domain (34.0°–35.0°N, 113.0°–114.0°E) covering region TRE and the period of 00:00 UTC 19 to 00:00 UTC 20 were chosen for the energy analysis.

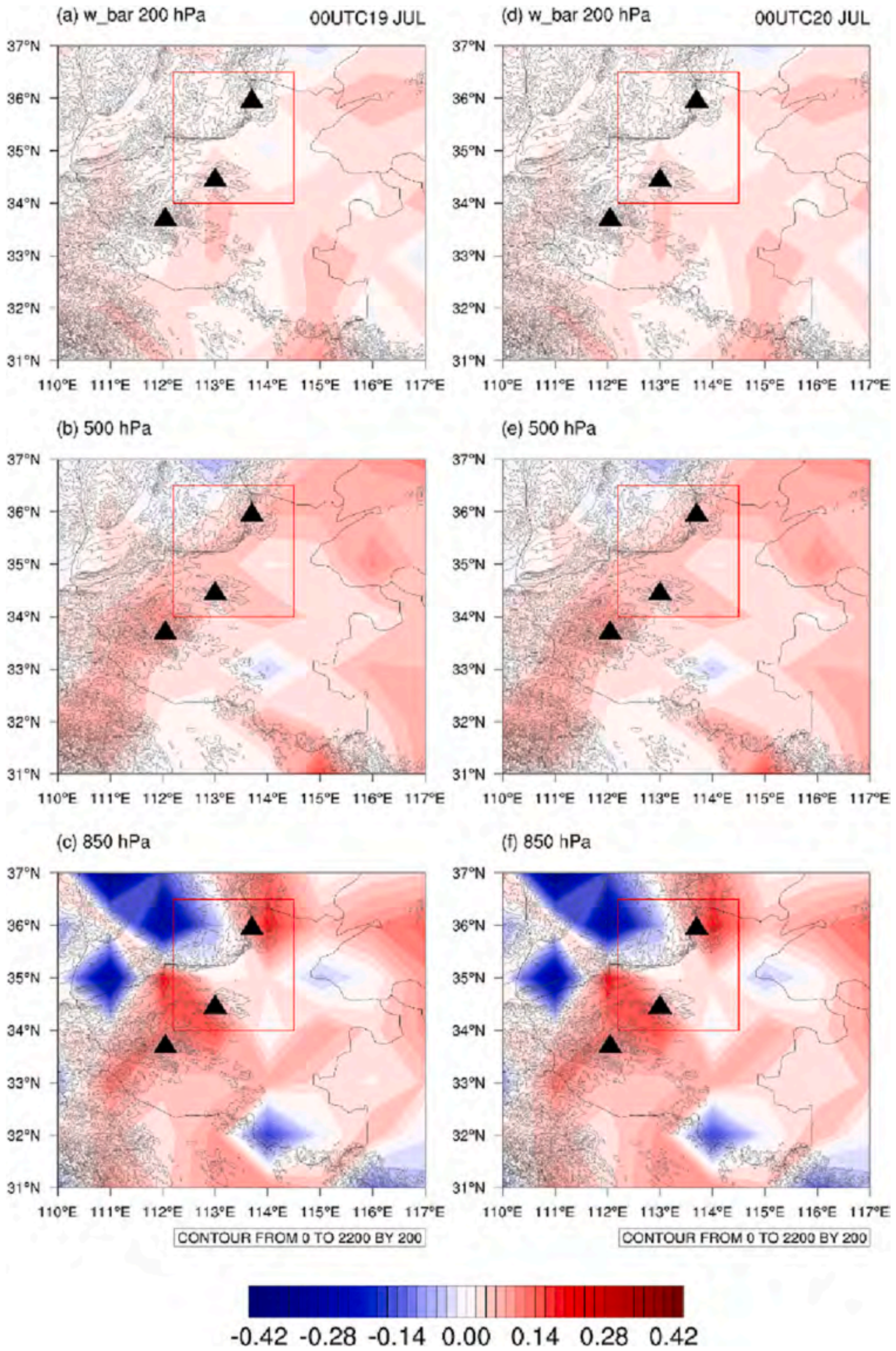

Fig. 7. The reconstructed vertical velocity (shaded; −1 × Pa/s) at (a, d) 200 hPa, (b, e) 500 hPa and (c, f) 850 hPa on July 19 (left column) and July 20 (right column) on the basic-flow scale (>64 days) obtained by using MWT. The grey contours are terrain height (m).

3.2. *Weather systems*

Fig. 2 shows the wind anomalies at 850 hPa and geopotential height anomalies at 500 hPa and 200 hPa. As can be seen, the geopotential height at 500 hPa (Fig. 2b, e) shows a positive anomalous belt in the mid-latitudes and a negative anomalous belt in the low latitudes. The large typhoon (In-Fa) in the Philippine Sea and the smaller typhoon (Cempaka) in the South China Sea were the two major weather systems in the low latitudes. At 850 hPa on July 19 (Fig. 2c), a cyclone was centered at (31.5°N, 114.05°E), with easterly flows in its north hitting the windward slopes of the Song, Funiu and Taihang mountains. The cyclone moved northwestwards and centered at (34°N, 112°E) with easterly and southeasterly flow converging over the trumpet-shaped topography of the Song and Funiu mountains on July 20 (Fig. 2f), which caused the exceptional rainstorm in Zhengzhou. On July 21, the cyclonic system moved northwards and hit the windward slopes of the Song Mountains, which caused the rainstorm in Anyang and Hebi (Fig. S2). Fig. 3 shows the vertically integrated water vaper flux and

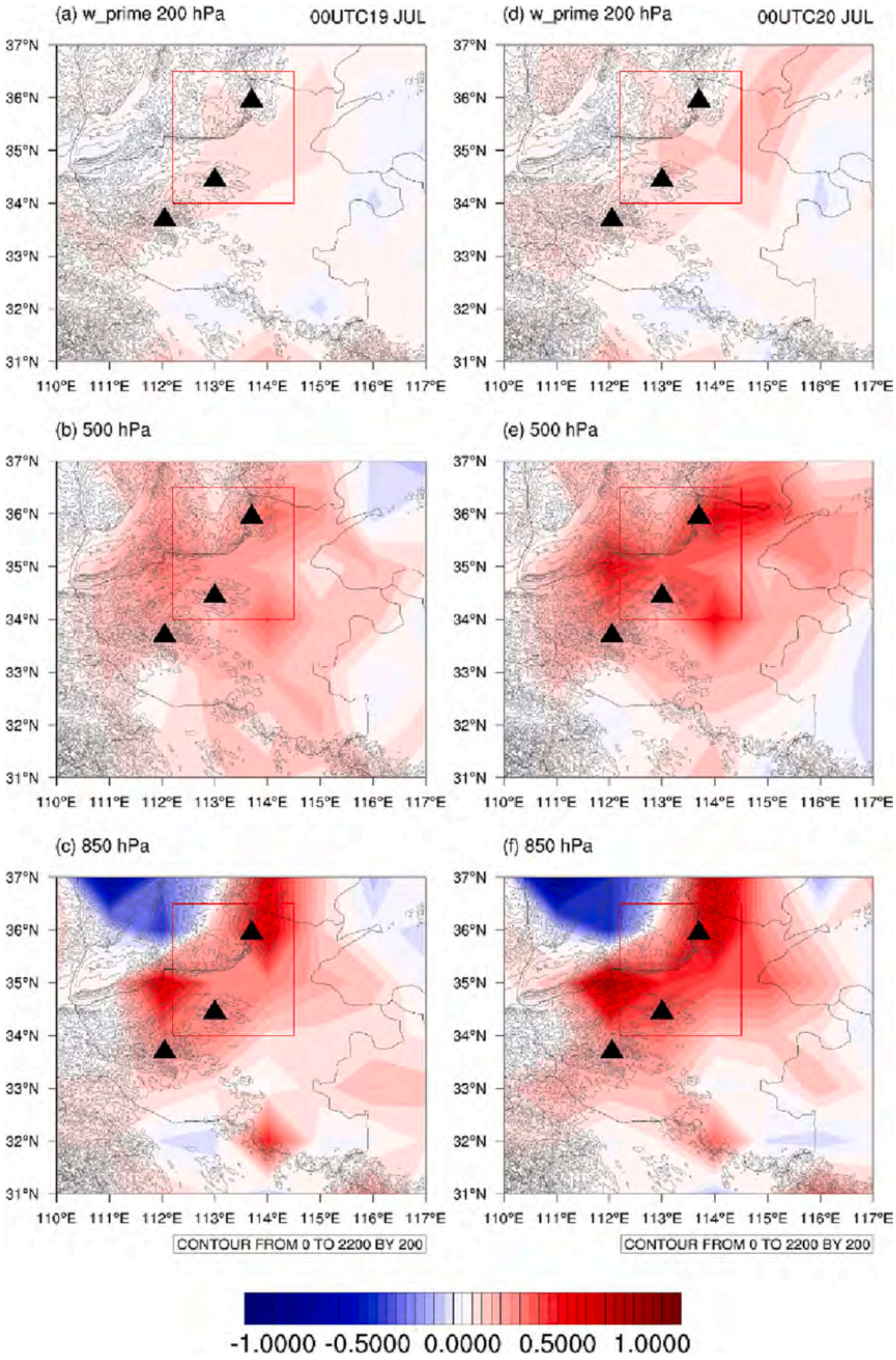

Fig. 8. As in Fig. 7 but for the reconstructed vertical velocity on the intraseasonal scale (8–64 days).

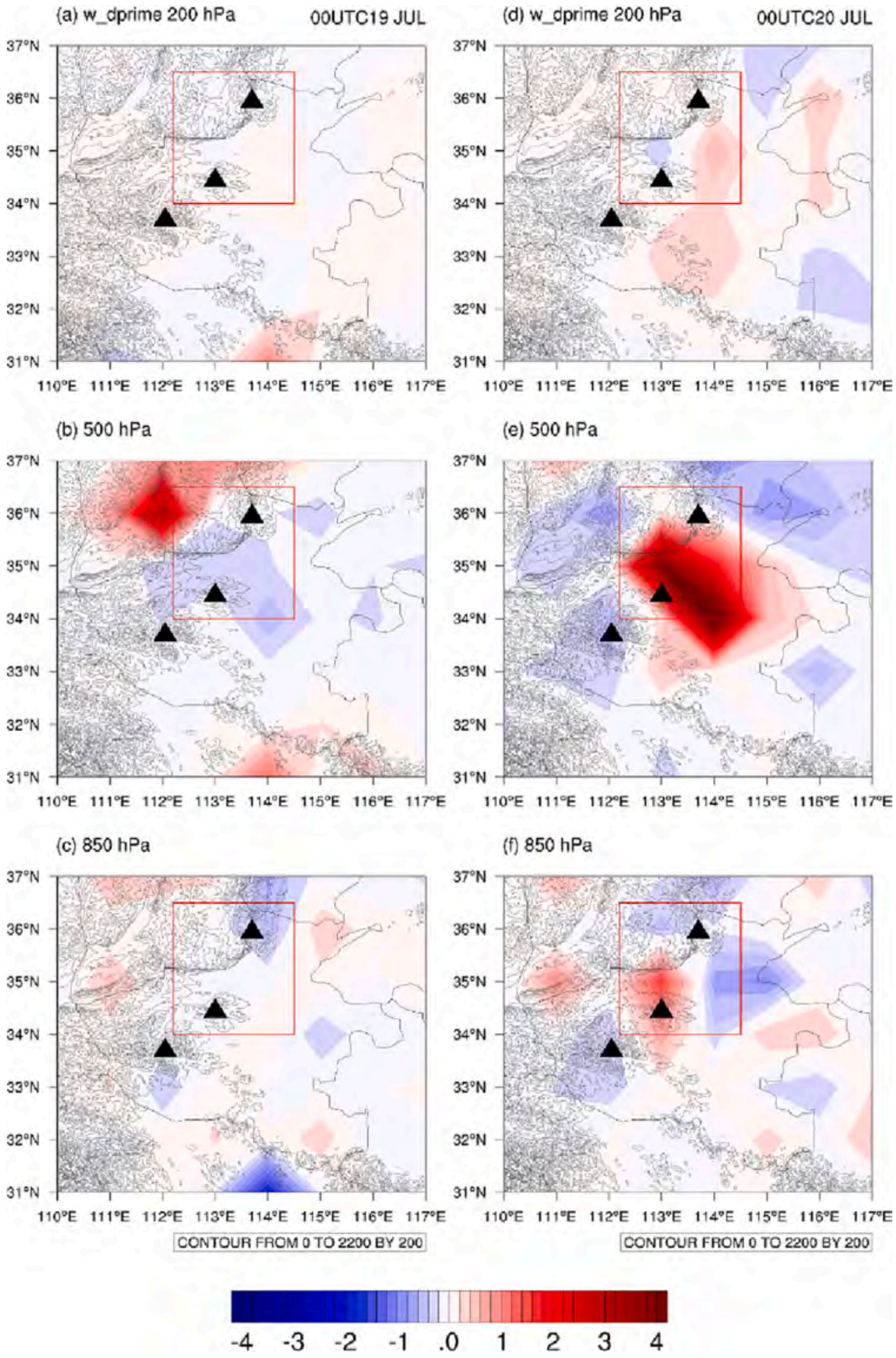

Fig. 9. As in Fig. 7 but for the reconstructed vertical velocity on the synoptic eddy scale (<8 days).

divergence averaged from July 19 to July 21. The water vapor was steadily transported to the Henan area by the easterly and southeasterly flow related to the peripheral flows around In-Fa, Cempaka, and the subtropical high to the north of In-Fa, which hit the Song and Funiu mountains, where they converged. The center of convergence was extremely prominent.

4. Multiscale energetics analysis

4.1. Multiscale reconstruction by MWT

The reconstructed basic flows are shown in Fig. 4. The basic flows are the same from 19 to 21 July, so only the basic flows on July 19 and 20 are shown. At 850 hPa, the height is low over land, high over the ocean, and a remarkably eastward-extended monsoon trough is situated over the western North Pacific. At 500 hPa, westerly flow is dominant at mid-latitudes, with a northwest–southeast-extended trough at 120°E. At 200

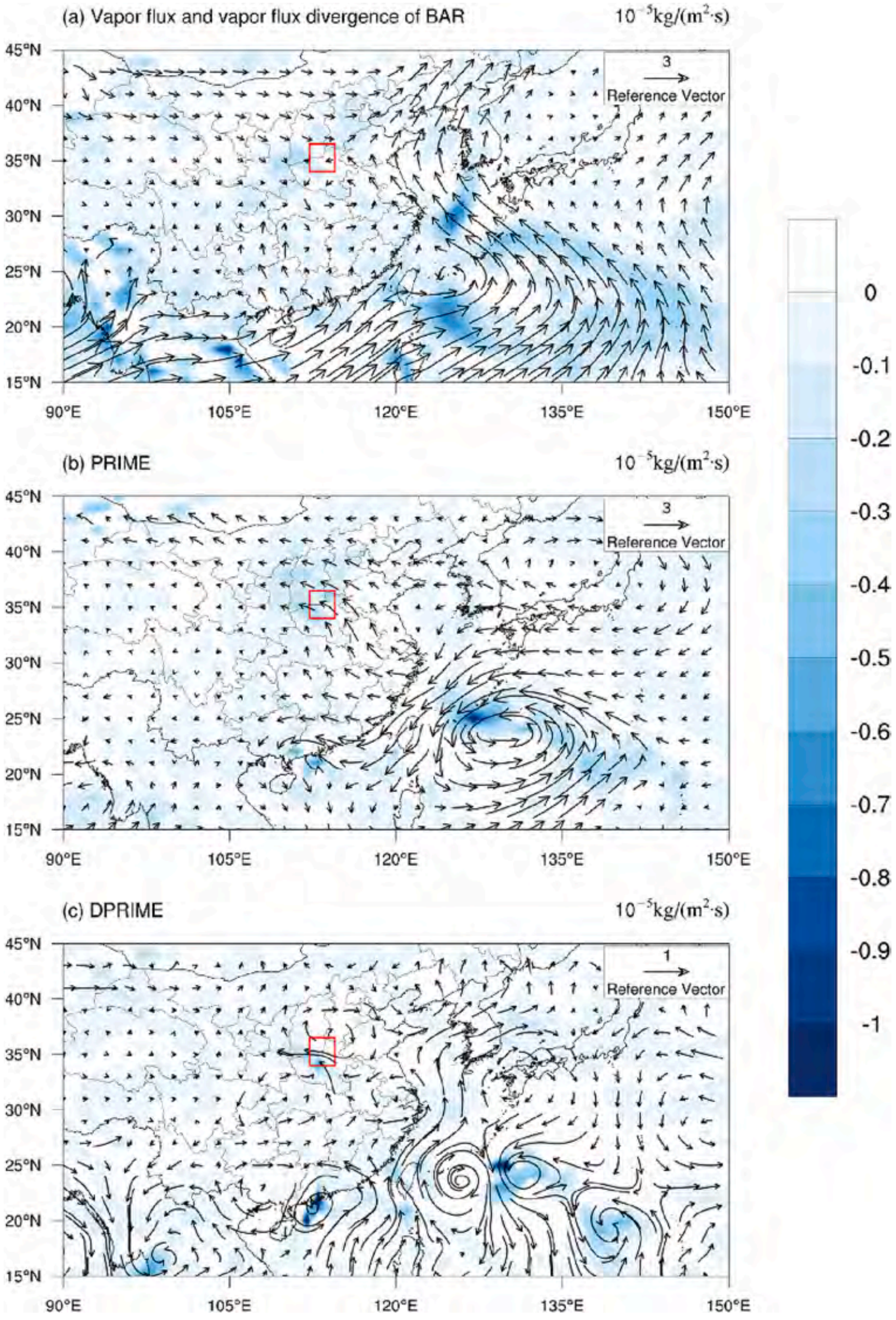

Fig. 10. The reconstructed vertically integrated water vapor flux (vectors; 100 kg/(m·s)) from 1000 hPa to 300 hPa and water vapor flux divergence (shaded; 10^{-5} kg/(m2·s)) averaged from July 19 to July 20 on the (a) basic-flow scale, (b) intraseasonal scale and (c) synoptic eddy scale. The red frames represent the TRE domain (34.0°–36.5°N, 112.0°–114.5°E). (For interpretation of the references to colour in this figure legend, the reader is referred to the web version of this article.)

Table 1
Vertically integrated water vapor flux along the borders the domain (34.0°–36.5°N, 112.0°–114.5°E), and the domain averaged divergence on three scales.

	Vapor flux $100kg/(m \bullet s)$							
Windows	Western border	Eastern border	East-west total	Northern border	Southern border	North-south total	Domain averaged Div.	Contribution
>64 days	0.17	−0.60	0.77	−0.56	−0.76	−0.2	−0.03	7.73%
8–64 days	−2.05	−2.88	0.83	1.74	2.31	0.57	−0.15	41.88%
< 8 days	−2.23	−2.42	0.19	0.57	1.98	1.41	−0.18	50.38%

hPa, the South Asian high covers the Tibetan Plateau and extends eastwards to the western North Pacific. The reconstructed intraseasonal flows are shown in Fig. 5, which to a certain extent reflect the synoptic systems shown in Fig. 2. Typhoon In-Fa in the western North Pacific and the subtropical high to its north are the two major weather systems both at 850 and 500 hPa. The rainstorm area is located at an inverted trough in the southeasterly flows prominent from 850 hPa to 200 hPa. The inverted trough resembles a Rossby wave, with a wavelength of approximately 2000 km in the easterlies at mid-latitudes, which may have been stimulated by Typhoon In-Fa. The inverted trough propagates westwards at 850 hPa and the TRE 21 is located in its front on July 19 (Fig. 5c), its center on July 20 (Fig. 5f), and its rear on July 21 (Fig. S3c). At 200 hPa, the cyclonic anomaly centered around (30°N, 102°E) suggests the South Asian high is weak. The reconstructed synoptic-scale systems reveal the synoptic eddy, as shown in Fig. 6. The prominent feature is a small-scale anticyclone with high pressure to the west of the westward-moving Typhoon In-Fa, which slows down the typhoon's speed of movement and results in water vapor being steadily transported to the area of the TRE (Fig. 6b, c, e, f). On July 19, an anticyclonic system at 850 hPa is located near the TRE domain, as shown in Fig. 6c. Saddle circulation is the feature at 200 hPa, with two cyclones straddling the west and east of the TRE domain and two anticyclones straddling its north and south. On July 20, the 850-hPa anticyclone is replaced by a cyclone in the TRE domain (Fig. 6f), along with prominent divergence at 200 hPa (Fig. 6d). On July 21, the cyclone at 850 hPa moves slowly to the north side of the TRE domain (Fig. S4c), accompanied by an

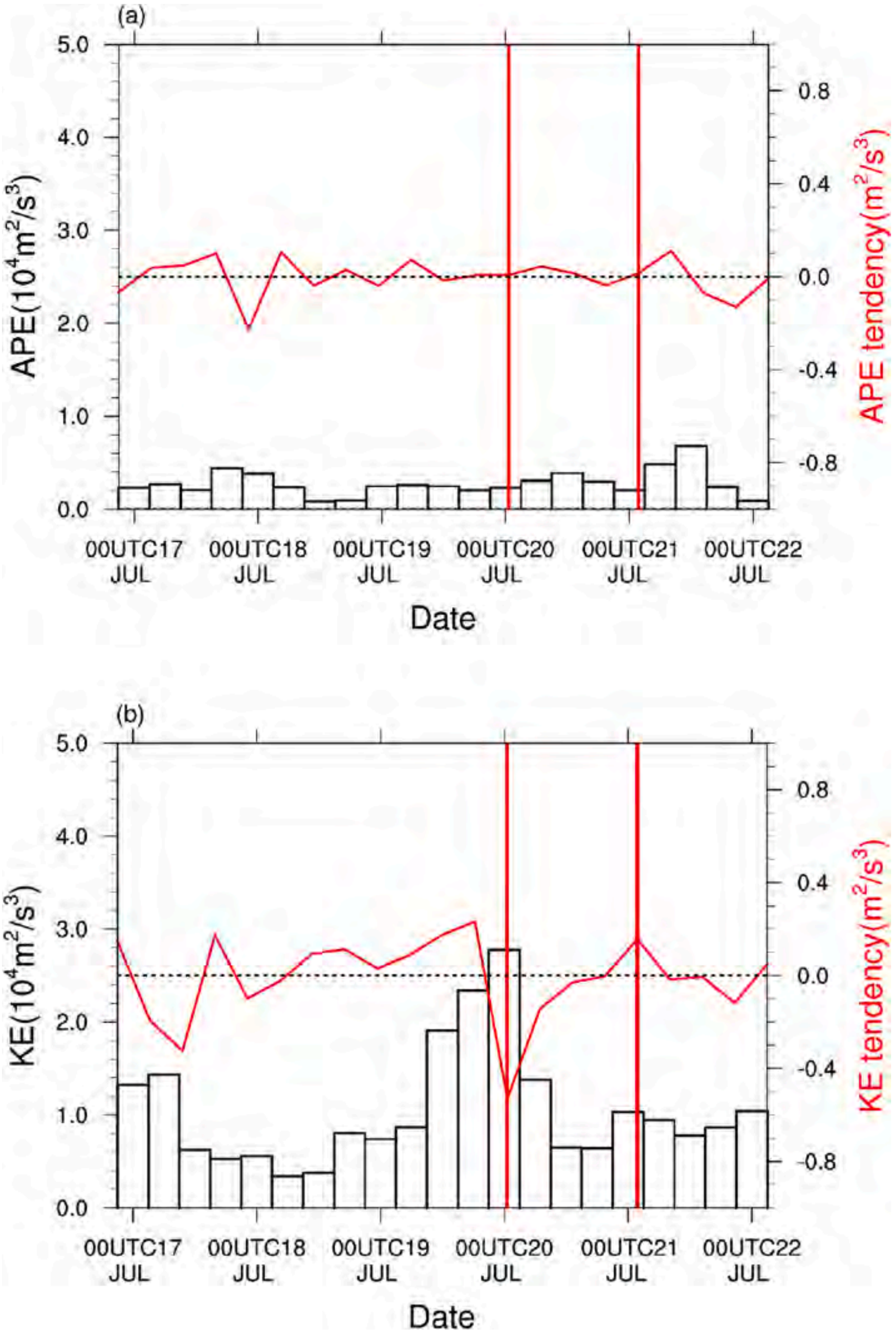

Fig. 11. Time series of APE and KE and their tendencies on the synoptic eddy scale integrated from 1000 to 100 hPa and averaged over the domain (34°–35°N, 113°–114°E): (a) APE (histogram; 10^4 m^2/s^2) and APE tendency (line; m^2/s^3); (b) KE (histogram; 10^4 m^2/s^2) and KE tendency (line; m^2/s^3).

anticyclone at the high level of 200 hPa (Fig. S4a).

The distributions of vertical velocity in the different scale windows are shown in Fig. 7 to Fig. 9. It is interesting that the prominent upward motions on the scale of basic flow remain unchanged and center over the east side of the Funiu and Taihang mountains (Fig. 7) at 850 hPa rather than at 500 hPa. This might be due to the uplift of the easterlies and southeasterlies as shown in Fig. 2c and f, and Fig. 4c and f, by the mountains. The uplift of the warm and wet airflow contribute to the occurrence and development of the rainstorm.

Fig. 8 shows the distribution of vertical velocity on the scale of 8–64 days. Notably, the magnitude of the vertical velocity on this scale is much larger than that on the scale of basic flow. The prominent upward motions on the scale of 8–64 days center over the east side of the Funiu and Taihang mountains at 850 hPa and enhance with time from July 19 to July 20. The maximum upward velocity is also prominent at 500 hPa, which is different to the 500-hPa vertical motion on the scale of basic flow. Moreover, another upward center near the Song Mountains is also prominent, which is perhaps due to the 500-hPa southerly on the scale of 8–64 days as shown in Fig. 5e and f, which is uplifted by these mountains. On the scale of the synoptic-scale eddy (Fig. 9), the vertical velocity is especially remarkable at 500 hPa on July 20, which is concurrent with the exceptional rainstorm at Zhengzhou. The question, however, is what happened on July 20? Was the exceptional rainstorm at Zhengzhou on this day related to barotropic or baroclinic instability?

To begin to address this question, we can examine the water vapor transport on the different scales. Fig. 10 shows the water vapor flux and water vapor flux divergence on the different scales averaged during July 19–20. On the scale of 8–64 days, the convergence is caused by southeasterlies. On the synoptic scale (< 8 days), southerlies converge with easterlies. As shown in Table 1, the east-westward convergence is prominent both on the scale of 8–64 days and > 64 days, which is $0.83\times$ and $0.77\times$ $100kg/(m\bullet s)$, while the south-northward convergence is prominent on the of scale of <8 days, which is $1.41\times$ $100kg/(m\bullet s)$. Over the TRE domain, the convergence of water vapor flux is prominent both on the scale of 8–64 days and $<$ 8 days, which contributing 41.88% and 50.38%, respectively.

4.2. *Analysis of energy transfer and transport based on MS-EVA*

a. **Evolution of the KE and APE on the synoptic scale**

Based on Eq. (3) and (4), the budget terms of the KE and APE on the synoptic scale can be obtained. Fig. 11 shows the time series of KE and APE and their tendency vertically integrated from 1000 hPa to 100 hPa and averaged over the domain of (34°–35°N, 113°–114°E) on the synoptic scale. We focus on the exceptional rainstorm process from 00:00 UTC 19 to 00:00 UTC 21. As shown in Fig. 11, on the synoptic eddy scale, the KE increases significantly from 12:00 until 24:00 on July 19, then drops significantly. The KE tendency is positive and increases gradually from 06:00 on July 19, before then dropping to a negative maximum at 00:00 on July 20 and thereafter increasing gradually. Contrary to the drastic fluctuation of KE, the APE and APE tendency do not change significantly; rather, the APE tendency remains positive during the occurrence of the exceptional rainstorm.

b. Energy transfer and transport on the scale of the rainstorm

Fig. 12a shows the time series of the vertically integrated and domain-averaged right-hand-side terms in Eq. (3) and (4). Although the APE and APE tendency change insignificantly during the occurrence of the exceptional rainstorm, the latent heating (represented by residual term) is largest prior to the exceptional rainstorm (at 06:00 UTC 20), which partially convert to KE through buoyancy term and partially transfer upscale (negative $\Gamma_A^{0\longrightarrow 2}$). It should be noted that there are persistent energy conversion from APE to KE on the synoptic scale prior to and during the occurance of the exceptional rainstorm (from 06:00 UTC 19 until 06:00 UTC 20), represented by negative buoyancy term. The prominent positive $\Gamma_A^{0\longrightarrow 2}$ during the occurrence of the exceptional

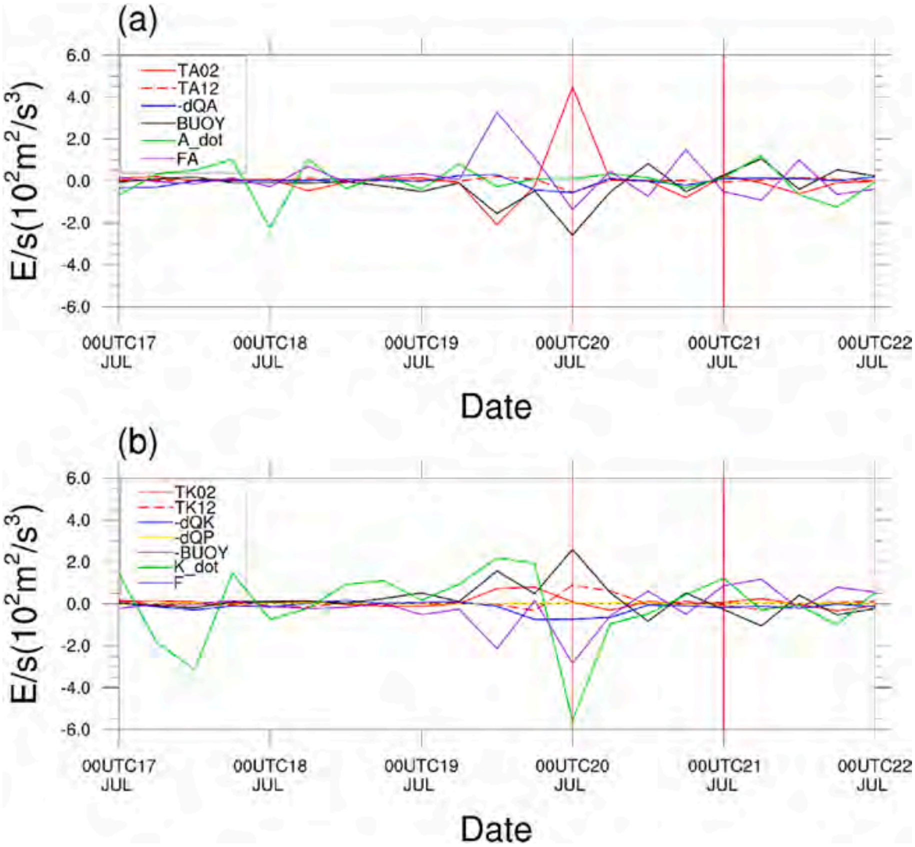

Fig. 12. Time series of the APE and KE budget terms (10^2 m^2/s^3) on the synoptic eddy scale integrated from 1000 to 100 hPa and averaged over the domain (34°–35°N, 113°–114°E). In (a), the red solid line is $\Gamma_A^{0\to 2}$; the red dashed line is $\Gamma_A^{1\to 2}$; the blue solid line is $-\nabla\bullet Q_A$; the black solid line is $-b^{\varpi}$; the green solid line is the APE tendency, which is multiplied by 10 to highlight the anomalies; and the purple line is the residual term. In (b), the red solid line is $\Gamma_K^{0\to 2}$; the red dashed line is $\Gamma_K^{1\to 2}$; the blue solid line is $-\nabla\bullet Q_K$; the yellow line is $-\nabla\bullet Q_P^{\varpi}$; the black solid line is b^{ϖ}; the green solid line is the KE tendency, which is multiplied by 10 to highlight the anomalies; and the purple line is the residual term. (For interpretation of the references to colour in this figure legend, the reader is referred to the web version of this article.)

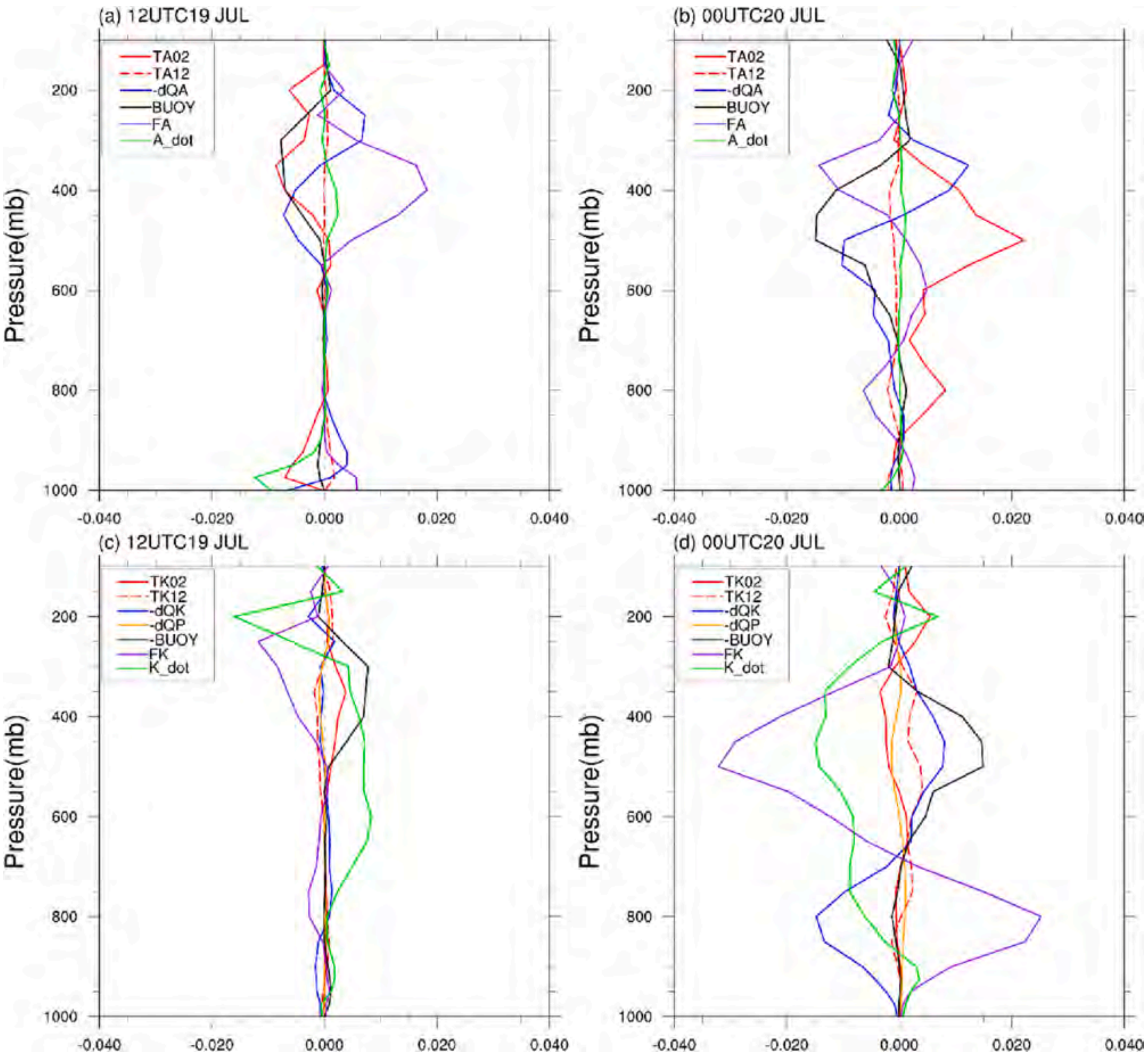

Fig. 13. Vertical profiles of APE (first row) and KE (second row) budget terms (m^2/s^3) and their tendencies on the synoptic eddy scale averaged over the domain (34°–35°N, 113°–114°E) at 12:00 UTC 19 (left column) and 00:00 UTC 20. The tendency of APE and KE is multiplied by 10 to highlight the anomalies.

rainstorm suggests a downscale energy cascade process of APE occurred and that it was largely balanced by the buoyancy term.

Fig. 12b shows the time series of the vertically integrated and domain-averaged right-hand-side terms in Eq. (4). The energy conversion from APE to KE from 06:00 UTC 19 until 06:00 UTC 20, represented by buoyancy, in addition to the barotropic energy transferring from the basic flow to synoptic eddy scale (positive $\Gamma_K^{0\longrightarrow 2}$ from 06:00 UTC 19 through 00:00 UTC 20), both contribute to the steady increase in KE during 06:00 UTC 19 to 18:00 UTC 19. Meanwhile, the KE is partially balanced by the divergence of the KE fluxes. The work done by the pressure gradient force contributes little to the KE of the rainstorm in this case.

But at which level did the prominent downscale or upscale energy cascade occur? Fig. 13 shows the vertical profile of the APE and KE budget terms on the scale of the rainstorm averaged over the domain (34°–35°N, 113°–114°E), where the rainstorm was centered.

At 12:00 UTC 19, prior to the exceptional rainstorm at Zhengzhou, F_A^2 is highly prominent at the levels of 300–500 hPa (Fig. 13a), which suggests that latent heating was the dominant contributor to the APE of the rainstorm. The latent heating (represented by residual term) at the levels of 300–500 hPa was largely balanced by buoyancy, in addtion to the divergence of the APE fluxes and energy cascade process of APE. An upscale energy cascade of APE occurs from the synoptic-eddy scale to the basic flow scale at the levels of 200–500 hPa (negative $\Gamma_A^{0\longrightarrow 2}$ in Fig. 13a). Near the surface, the upscale energy cascade of APE is largely offset by positive values of F_A^2 near the surface, which is perhaps related to the sensible heating, and contributes to the negative APE tendency near the surface. As shown in Fig. 13c, both the buoyancy and positive $\Gamma_K^{0\longrightarrow 2}$ contribute to the KE positive tendency at the levels of 300–500 hPa; however, they are mostly balanced by the residual term of KE, i.e., F_K^2, which represents the work done by eddy dissipation and diffusion.

At 00:00 UTC 20, buoyancy term was prominent negative at the levels of 350–600 hPa (Fig. 13b). This denotes the ascent of warm air and descent of cold air, and the APE conversion to KE on the scale of the synoptic eddy. A downscale energy cascade of APE from the basic flow to the synoptic-eddy scale, i.e., $\Gamma_A^{0\longrightarrow 2}$, was also prominent at the same levels which is mostly balanced by the negative buoyancy. The previous latent heating at the levels of 300–500 hPa decreases significantly,

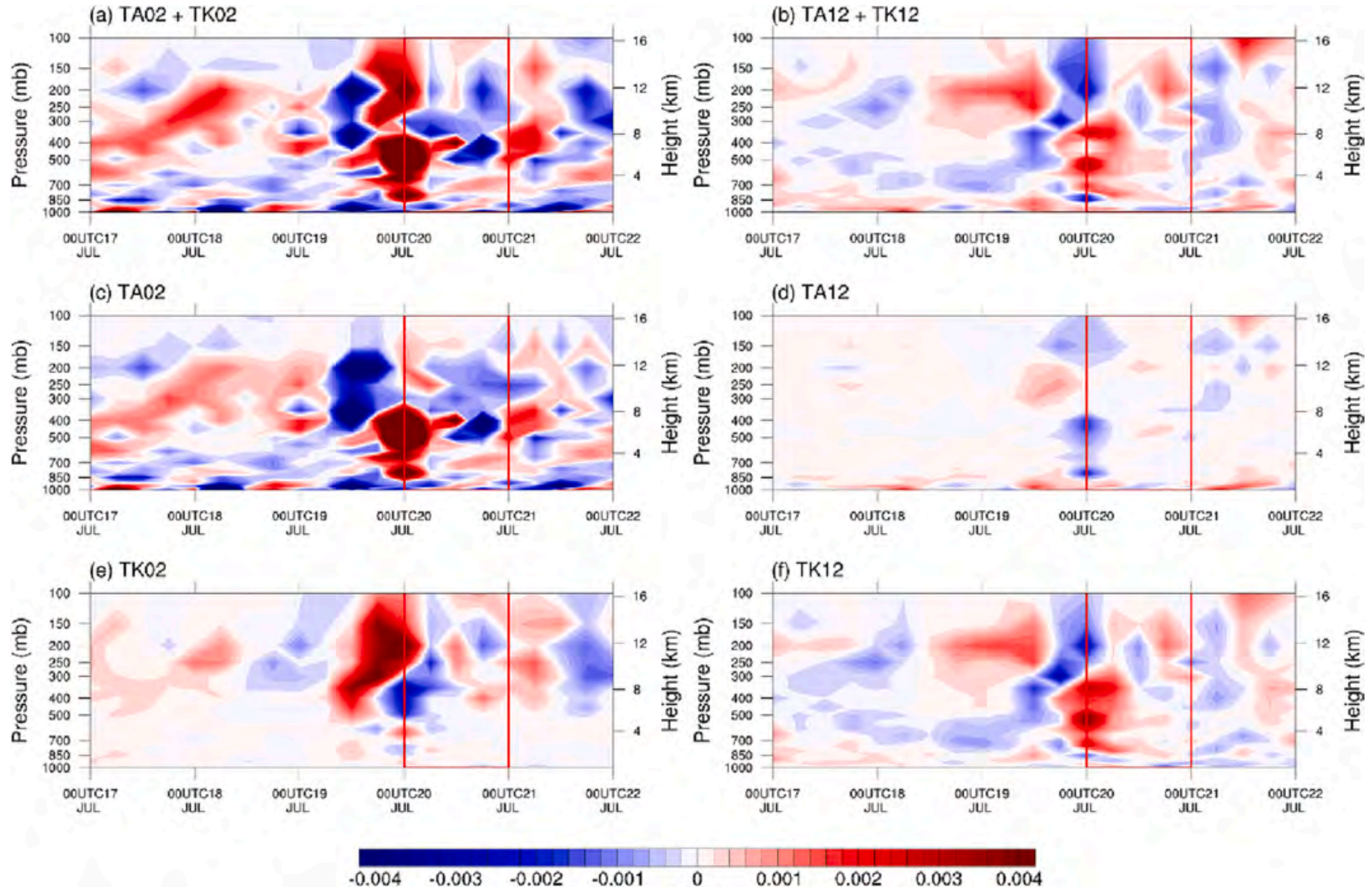

Fig. 14. Time–height distributions of (c) $\Gamma_A^{0\longrightarrow2}$, (d) $\Gamma_A^{1\longrightarrow2}$, (e) $\Gamma_K^{0\longrightarrow2}$, and (f) $\Gamma_K^{1\longrightarrow2}$, and (a, b) their sums, averaged over the domain (34°–35°N, 113°–114°E).

occurs at the levels of 450–700 hPa, and is largely balanced by the divergence of the APE fluxes and the negative buoyancy. For the KE budget profile (Fig. 13d), the KE tendency is negative from the surface to 250 hPa, which is contributed by the divergence of the KE fluxes from the surface to 700 hPa and largely balanced by the residual term of the KE budget, which represents the work done by the eddy. At the levels of 300–700 hPa, a negative residual term of the KE budget occurs and is largely balanced by the buoyancy and the convergence of the KE fluxes.

In summary, the buoyancy conversion remained prominent at the middle and upper levels, which imply persistent energy conversion from APE to KE (represented by the buoyancy term) prior to and during the occurance of the exceptional rainstorm, and caused a noticeable increase in KE, while the APE and APE tendency change insignificantly. Prior to the occurance of the exceptional rainstorm, the diabatic heating was the main source of APE which was largely balanced by buoyancy, the divergence of the APE fluxes and energy cascade process of APE. In addition to buoyancy conversion, a downscale energy cascade process of KE (barotropic instability) was another source of KE prior to the rainstorm; During the rainstorm's occurrence, the downscale energy cascade process of APE was the major source of APE which was largely balanced by buoyancy. KE decreased significantly owing to eddy dissipation and diffusion at middle levels and the divergence of KE fluxes at low levels. The work done by the pressure gradient force was negligible for KE.

c. Barotropic and baroclinic instability during the rainstorm

Fig. 14 shows the time–height distribution of $\Gamma_A^{0\longrightarrow2}$, $\Gamma_K^{0\longrightarrow2}$, $\Gamma_A^{1\longrightarrow2}$, $\Gamma_K^{1\longrightarrow2}$ and their sum averaged over the domain (34°–35°N, 113°–114°E) during the rainstorm process. As shown in Fig. 14a, $\Gamma_K^{0\longrightarrow2} + \Gamma_A^{0\longrightarrow2} > 0$ from low to high levels from 18:00 UTC 19 to 06:00 UTC 20, which indicates the basic flow was locally unstable. Moreover, $\Gamma_A^{0\longrightarrow2} > 0$ and $\Gamma_K^{0\longrightarrow2} < 0$ from 400 to 850 hPa (Fig. 14c, e) indicate baroclinic instability related to the vertical shear of zonal wind at the low and middle levels on the basic flow scale, as shown in Fig. 4. A few hours earlier, $\Gamma_K^{0\longrightarrow2}$ is significantly positive above 400 hPa, which indicates that locally the basic flow was barotropic instability, due to the horizontal shear of wind above 400 hPa as shown in Fig. 4a and 4d.

Fig. 14b, d and f show the energy transfers from the scale of 8–64 days to the scale of the rainstorm, which are much weaker than those from the scale of the basic flow. However, the instability occurring in the low and middle layers, with $\Gamma_A^{1\longrightarrow2} + \Gamma_K^{1\longrightarrow2} > 0$ and $\Gamma_A^{1\longrightarrow2} < 0$, $\Gamma_K^{1\longrightarrow2} > 0$ during 18:00 UTC 19 to 06:00 UTC 20, indicates the flow on the scale of 8–64 days is barotropic instability related to the horizontal shear of wind at low and middle layers on the scale of 8–64 days, as shown in Fig. 5.

Fig. 15 shows the height–longitude profiles of $\Gamma_A^{0\longrightarrow2}$, $\Gamma_K^{0\longrightarrow2}$, $\Gamma_A^{1\longrightarrow2}$, $\Gamma_K^{1\longrightarrow2}$ at averaged latitudes (34°–35°N) and averaged times from 06:00 UTC 19 to 18:00 UTC 19 and 18:00 UTC 19 to 06:00 UTC 20, separately.

As can be seen, from 400 to 850 hPa, $\Gamma_A^{0\longrightarrow2} > 0$, $\Gamma_K^{0\longrightarrow2} < 0$ and $\Gamma_K^{0\longrightarrow2} + \Gamma_A^{0\longrightarrow2} > 0$, averaged from 18:00 UTC 19 to 06:00 UTC 20 (Fig. 15 a2, c2 and e2), which indicates the basic flow was locally unstable and the instability was baroclinic at low and middle levels. A few hours earlier, $\Gamma_K^{0\longrightarrow2}$ is significantly positive above 400 hPa (Fig. 15e1), which indicates the basic flow was locally barotropically unstable.

From 400 to 850 hPa and averaged from 18:00 UTC 19 to 06:00 UTC 20, $\Gamma_A^{1\longrightarrow2} < 0$, $\Gamma_K^{1\longrightarrow2} > 0$ and $\Gamma_A^{1\longrightarrow2} + \Gamma_K^{1\longrightarrow2} > 0$ (Fig. 15 b2, d2 and f2), which indicates the flow on the scale of 8–64 days was barotropically unstable in the low and middle layers.

These results further verify that baroclinic instability at middle levels on the scale of the basic flow, barotropic instability at the upper levels on the scale of the basic flow, and barotropic instability at lower levels on the scale of 8–64 days, were the main energy sources of this storm

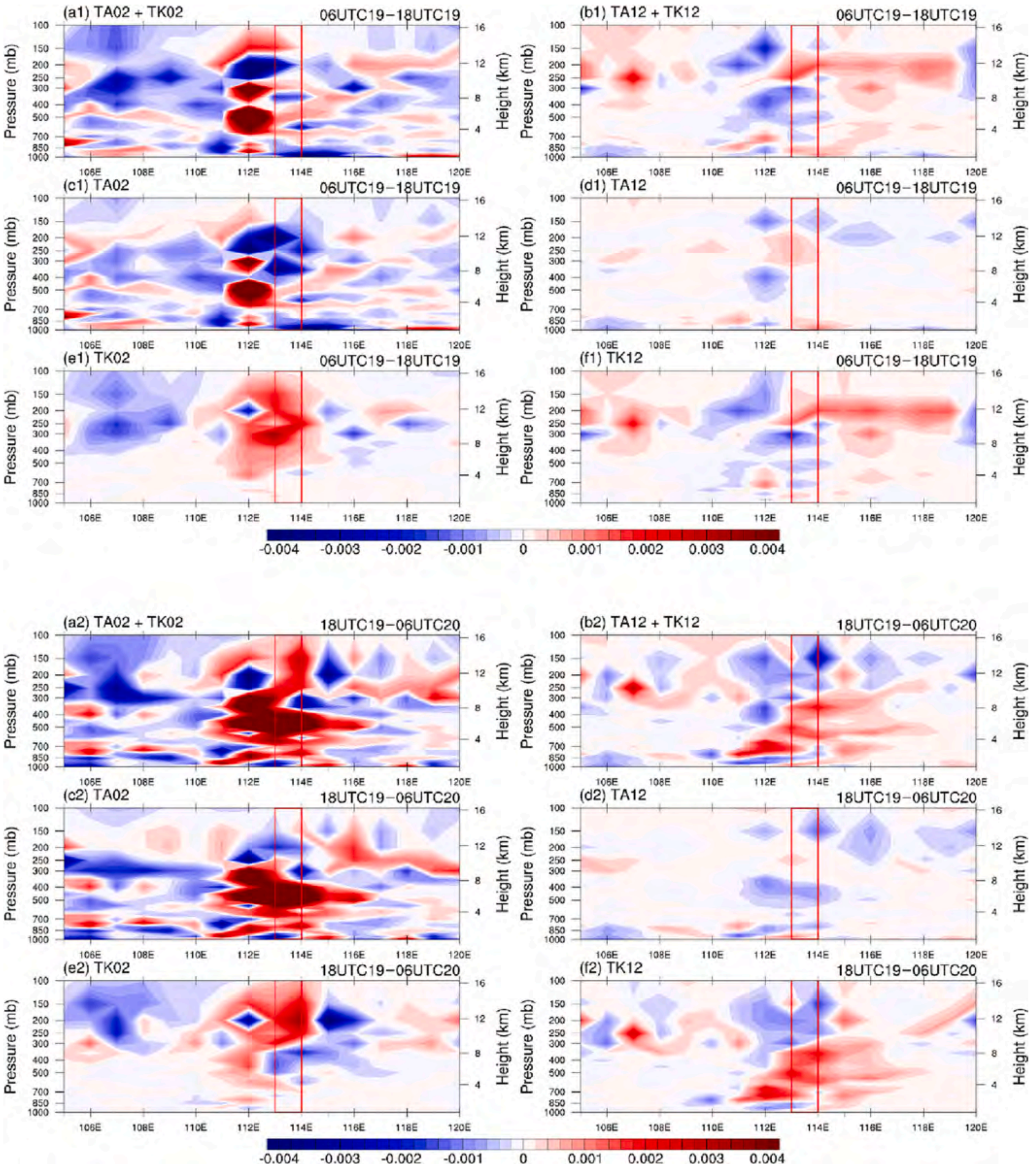

Fig. 15. Height–longitude profiles of (c1, c2) $\Gamma_A^{0\longrightarrow2}$, (d1, d2) $\Gamma_A^{1\longrightarrow2}$, (e1, e2) $\Gamma_K^{0\longrightarrow2}$, (f1, f2) $\Gamma_K^{1\longrightarrow2}$ and (a1, a2, b1, b2) their sums, at averaged latitudes (34°–35°N) and averaged times from (a1–f1) 06:00 UTC 19 to 18:00 UTC 19 and (a2–f2) 18:00 UTC 19 to 06:00 UTC 20.

process.

5. Discussion and conclusions

Based on the MWT and MWT-based localized and instantaneous multiscale energetics analysis methodology developed by Liang and Anderson (2007), we examined the multiscale dynamical processes and energy sources of the 21•7 TRE, especially the exceptional rainstorm that hit Zhengzhou on July 20, 2021.

By applying MWT, we decomposed and reconstructed the reanalysis fields from the NCEP FNL dataset into three temporal scales: a background window (>64 days); an intraseasonal-scale window (8–64 days); and a synoptic-eddy-scale window (<8 days). The results showed that the rainstorm occurred in an inverted trough on the scale of 8–64 days, which may have been stimulated by Typhoon In-Fa in the easterly flow. A small high-pressure system to the west of the westward-moving Typhoon In-Fa, as shown in the circulation on that scale of the synoptic eddy, slowed down the moving speed of Typhoon In-Fa, resulting in a steady transportation of water vapor. This, in addition to the uplift caused by the trumpet-shaped topography of the Taihang and Niushou mountains, as revealed by the vertical motion at 850 hPa on the scale of the basic flow, caused the persistent and exceptional rainstorm.

By applying MS-EVA diagnosis, we found there were persistent energy conversion from APE to KE represented by the buoyancy term both prior to and during the occurrence of the exceptional rainstorm at Zhengzhou, while the work done by the pressure gradient force was negligible. Prior to the rainstorm, the latent heating was the important sources of APE, and a downscale energy cascade process of KE (barotropic instability) above 500 hPa was the important sources of KE besides the buoyancy term. During the rainstorm's occurrence, KE decreased significantly owing to eddy dissipation and diffusion at middle levels and the divergence of KE fluxes at low levels, while the downscale energy cascade process of APE (baroclinic instability) at middle levels was the source of APE, which was largely balanced by the buoyancy term. The barotropic instability at lower levels on the scale of 8–64 days, were another major energy sources of this storm.

Hsu et al. (2023) decomposed fields into four scales by using Lanczos bandpass filter and analyzed the moisture budget equation on differrnt scales during 21•7 TRE. They found that the boreal summer intraseasonal oscillation (10–30 and 30–90 days) unusually had a crucial combined role in moisture convergence during 21•7 TRE. But it is difficult to strictly decompose fields into different scales with traditional filter such as Lanczos bandpass filter, let alone conduct quantitative analysis of the multiscale interaction between different scales.

In this study, we applied recently developed MWT and to decompose and reconstruct the total field and identified the systems in different scales. Then, we quantitatively diagnosed the energy transfer between different scales in order to understand the underlying dynamical processes. The persistent energy conversion from APE to KE in the last 12 h and throughout the occurrence of the TRE are exceptional. Prior to the rainstorm, the latent heating was the important sources of APE. During the rainstorm's occurrence, the downscale energy cascade process of APE at middle levels was the source of APE, which implied that multiscale interaction may be the main reason for the event's extremity.

Though these findings nevertheless help us in better understanding the dynamics of this exceptional rainstorm and the interactions between the three scales, it should be noted that the $1.0^\circ \times 1.0^\circ$ and 6-hourly resolutions of FNL data is fairly coarse in describing the extremity of the 21•7 TRE. The multiscale interactions and dynamics of 21•7 TRE may be varied using higher spatial and temporal resolution data.

CRediT authorship contribution statement

Jiayi Liu: Investigation, Data curation, Visualization, Writing - original draft. **Li Tao:** Investigation, Conceptualization, Methodology, Supervision, Writing - review & editing. **Yang Yang:** Writing – review & editing.

Declaration of Competing Interest

The authors declare the following financial interests/personal relationships which may be considered as potential competing interests:

Tao Li reports article publishing charges was provided by State Key Laboratory of Severe Weather, Chinese Academy of Meteorological Sciences. Tao Li reports a relationship with State Key Laboratory of Severe Weather, Chinese Academy of Meteorological Sciences that includes: funding grants.

Data availability

Data will be made available on request.

Acknowledgements

This work was funded by the Open Grants of the State Key Laboratory of Severe Weather under grant 2022LASW-B07 and the National Natural Science Foundation of China (NSFC) under grant 42230105. Yang is supported by the NSFC under Grants 42276017 and 41975064.

Appendix A. Supplementary data

Supplementary data to this article can be found online at https://doi.org/10.1016/j.atmosres.2023.106857.

References

Barnes, S.L., 1964. A technique for maximizing details in numerical weather map analysis. J. Appl. Meteorol. Climatol. 3, 396–409. https://doi.org/10.1175/1520-0450(1964)003<0396:ATFMDI>2.0.CO;2.

Deng, L., Feng, J.N., Zhao, Y., et al., 2022. The remote effect of binary typhoon Infa and Cempaka on the "21.7" heavy rainfall in Henan province, China. J. Geophys. Res.-Atmos. 127 https://doi.org/10.1029/2021JD036260 e2021JD036260.

Ding, Y.H., 2014. Contributions of Prof. Shiyan Tao to the study of formation conditions and mechanisms of heavy rainfall in China (in Chinese). Chin. J. Atmos. Sci. 38, 616–626. https://doi.org/10.3878/j.issn.1006-9895.2013.13226.

Fu, S.M., Wang, H.J., Sun, J.H., et al., 2016. Energy budgets on the interactions between the mean and eddy flows during a persistent heavy rainfall event over the Yangtze River valley in summer 2010. J. Meteorol. Res. 30, 513–527. https://doi.org/10.1007/s13351-016-5121-3.

Fu, S.M., Zhang, Y.C., Wang, H.J., et al., 2022. On the evolution of a long-lived mesoscale convective vortex that acted as a crucial condition for the extremely strong hourly precipitation in Zhengzhou. J. Geophys. Res.-Atmos. 127 https://doi.org/10.1029/2021JD036233 e2021JD036233.

Hersbach, H., Bell, B., Berrisford, P., et al., 2020. The ERA5 global reanalysis. Q. J. R. Meteorol. Soc. 146, 1999–2049. https://doi.org/10.1002/qj.3803.

Hsu, P.C., Li, T., 2011. Interactions between boreal summer intraseasonal oscillations and synoptic-Scale disturbances over the Western North Pacific. Part II: Apparent heat and moisture sources and eddy momentum transport. J. Clim. 24, 942–961. https://doi.org/10.1175/2010JCLI3834.1.

Hsu, P.C., Xie, J.H., Lee, J.Y., et al., 2023. Multiscale interactions driving the devastating floods in Henan Province, China during July 2021. Weather Clim. Extrem. 39, 100541 https://doi.org/10.1016/j.wace.2022.100541.

Hu, S., Zhou, T., Wu, B., et al., 2023. Seasonal prediction of the record-breaking northward shift of the Western Pacific Subtropical High in July 2021. Adv. Atmos. Sci. 40, 410–427. https://doi.org/10.1007/s00376-022-2151-x.

Liang, X.S., 2016. Canonical transfer and multiscale energetics for primitive and quasigeostrophic atmospheres. J. Atmos. Sci. 73, 4439–4468. https://doi.org/10.1175/JAS-D-16-0131.1.

Liang, X.S., Anderson, D.G.M., 2007. Multiscale window transform. Multisc. Model. Simul. 6, 437–467. https://doi.org/10.1137/06066895X.

Liang, X.S., Robinson, A.R., 2005. Localized multiscale energy and vorticity analysis: I. Fund. Dynam. Atmos. Oceans. 38, 195–230. https://doi.org/10.1016/j.dynatmoce.2004.12.004.

Liang, X.D., Xia, R.D., Bao, X.H., et al., 2022. Preliminary investigation on the extreme rainfall event during July 2021 in Henan Province and its multi-scale processes (in Chinese). Chin. Sci. Bull. 67, 997–1011. https://doi.org/10.1360/TB-2021-0827.

Luo, Y., Du, Y., 2023. The roles of low-level jets in "21·7" Henan extremely persistent heavy rainfall event. Adv. Atmos. Sci. 40, 350–373. https://doi.org/10.1007/s00376-022-2026-1.

Majda, A.J., Stechmann, S.N., 2009. A simple dynamical model with features of convective momentum transport. J. Atmos. Sci. 66, 373–392. https://doi.org/10.1175/2008JAS2805.1.

Ran, L.K., Li, S.W., Zhou, Y.S., et al., 2021. Observational analysis of the dynamic, thermal, and water vapor characteristics of the "7.20" extreme rainstorm event in Henan Province, 2021 (in Chinese). Chin. J. Atmos. Sci. 45, 1366–1383. https://doi.org/10.3878/j.issn.1006-9895.2109.21160.

Sha, S., Shen, X.Y., Li, X.F., 2018. The study of multi-scale energy interactions during a Meiyu Front rainstorm. Part II: Practical application (in Chinese). Chin. J. Atmos. Sci. 42, 1119–1132. https://doi.org/10.3878/j.issn.1006-9895.1710.17196.

Shen, X.Y., Sha, S., Liu, L.K., 2018a. Research progress on atmospheric multiscale interaction (in Chinese). Torrenti. Rain Disast. 37, 197–203. https://doi.org/10.3969/j.issn.1004-9045.2018.03.001.

Shen, X.Y., Sha, S., Li, X.F., 2018b. The study of multi-scale energy interactions during a Meiyu Front rainstorm. Part I: theoretical analysis (in Chinese). Chin. J. Atmos. Sci. 42, 1109–1118. https://doi.org/10.3878/j.issn.1006-9895.1710.17195.

Tao, S.Y., 1980. Heavy Rains in China (in Chinese). Science Press, Beijing.

Wei, P., Xu, X., Xue, M., et al., 2023. On the key dynamical processes supporting the 21.7 Zhengzhou record-breaking hourly rainfall in China. Adv. Atmos. Sci. 40, 337–349. https://doi.org/10.1007/s00376-022-2061-y.

Xu, H.X., Duan, Y.H., Xu, X.D., 2022. Indirect effects of binary typhoons on an extreme rainfall event in Henan province, China from 19 to 21 July 2021: 2. Numerical study. J. Geophys. Res.-Atmos. 127 https://doi.org/10.1029/2021JD036083 e2021JD036083.

Yu, Y., Gao, T., Xie, L., et al., 2022. Tropical cyclone over the western Pacific triggers the record-breaking '21/7' extreme rainfall in Henan, Central-Eastern China. Environ. Res. Lett. 17, 124003 https://doi.org/10.1088/1748-9326/aca2c4.

Zhang, X., Wang, Y.Q., Wang, J., et al., 2008. Impact analysis of interaction between Typhoon "Haitang" and mid-latitude systems on rainstorm in Henan (in Chinese). Meteorol. Sci. Technol. 36, 55–62. https://doi.org/10.19517/j.1671-6345.2008.01.012.

Zhang, X., Yang, H., Wang, X.M., et al., 2021. Analysis on characteristic and abnormality of atmospheric circulations of the July 2021 extreme precipitation in Henan (in Chinese). Trans. Atmos. Sci. 44, 672–687. https://doi.org/10.13878/j.cnki.dqkxxb.20210907001.

Zhang, G., Mao, J., Hua, W., et al., 2023. Synergistic effect of the planetary-scale disturbance, typhoon and meso-β-scale convective vortex on the extremely intense rainstorm on 20 July 2021 in Zhengzhou. Adv. Atmos. Sci. 40, 428–446. https://doi.org/10.1007/s00376-022-2189-9.

Zhao, P., Sun, J., Zhou, X.J., 2003. Mechanism of formation of low level jets in the South China Sea during spring and summer of 1998. Chin. Sci. Bull. 48, 1265–1270. https://doi.org/10.1007/BF03183949.